Wavelet Operators and Multiplicative Observation Models -Application to SAR Image Time Series Analysis

Abdourrahmane Atto, Emmanuel Trouvé, Jean-Marie Nicolas, Thu Trang Lê

Wavelet Operators and Multiplicative Observation Models - Application to SAR Image Time Series Analysis

Abdourrahmane M. Atto[1,*], Emmanuel Trouvé[1], Jean-Marie Nicolas[2], Thu-Trang Lê[1]

***Abstract*—This paper first provides statistical properties of wavelet operators when the observation model can be seen as the product of a deterministic piecewise regular function (signal) and a stationary random field (noise). This multiplicative observation model is analyzed in two standard frameworks by considering either (1) a direct wavelet transform of the model or (2) a log-transform of the model prior to wavelet decomposition. The paper shows that, in Framework (1), wavelet coefficients of the time series are affected by intricate correlation structures which blur signal singularities. Framework (2) is shown to be associated with a multiplicative (or geometric) wavelet transform and the multiplicative interactions between wavelets and the model highlight both sparsity of signal changes near singularities (dominant coefficients) and decorrelation of speckle wavelet coefficients. The paper then derives that, for time series of synthetic aperture radar data, geometric wavelets represent a more intuitive and relevant framework for the analysis of smooth earth fields observed in the presence of speckle. From this analysis, the paper proposes a fast-and-concise geometric wavelet based method for joint change detection and regularization of synthetic aperture radar image time series. In this method, geometric wavelet details are first computed with respect to the temporal axis in order to derive generalized-ratio change-images from the time series. The changes are then enhanced and speckle is attenuated by using spatial block sigmoid shrinkage. Finally, a regularized time series is reconstructed from the sigmoid shrunken change-images. Some applications highlight relevancy of the method for the analysis of SENTINEL-1A and TerraSAR-X image time series over Chamonix-Mont-Blanc.**

***Index Terms*—Wavelets ; Geometric convolution ; Synthetic Aperture Radar ; Image Time Series Analysis.**

I. Introduction - Motivation

SYNTHETIC Aperture Radar (SAR) image time series issued from new generation sensors show minute details. Indeed, the evolution of SAR imaging systems is such that in less than 2 decades:

- high resolution sensors can achieve metric resolution, providing richer spatial information than the decametric data issued from ERS or ENVISAT missions.
- the earth coverage has increased: recent satellites such as TerraSAR-X and Sentinel-1A repeat their cycle in a dozen of days.

The increase of those spatial and temporal resolutions makes information extraction tricky from highly resolved SAR image time series. This compels us *re-considering data features and representations in order to simplify data processing.*

The paper presents a parsimonious framework for the analysis of huge data associated with multiplicative type interactions. These data are observed in many situations, for instance when acquiring signals from radar/sonar/ultrasonic waves [1]/[2]/[3],[4], when analyzing seasonality from meteorology data [5] or when focusing on proportionality in economy data [6] and political sciences [7]. We focus specifically on SAR systems, a challenging imagery domain with huge amount of data affected by multiplicative type interactions.

From the literature, analysis of SAR image time series has been mainly performed on short-length image sequences. This is the consequence of SAR data cost (very high), long satellite revisit time and short satellite lifetime, among other issues. Literature concerns both theoretical and application guided methods for:

- identifying appropriate statistics/similarity measures [8], [9], [10], [11], [12], [13], [14], [15], [16], [17], *etc.*;
- detecting and analyzing specific features, for instance urban areas expansion [8], [18], [19], glaciers dynamics [13], [20], [21], snow cover mapping [22], sea clutter analysis [23], forest mapping [24], earthquake monitoring [8], sea ice motion analysis [25], coastline detection [26], soil erosion [27], *etc.*;
- regularizing SAR data for speckle reduction and feature enhancement [19], [24], [26], [28], [29].

[1] LISTIC, EA 3703, Université Savoie Mont Blanc - Université Grenoble Alpes, France
[2] LTCI, CNRS UMR 5141, Telecom ParisTech, 46 rue Barrault, 75013 Paris, France
* Corresponding author, Email: *Abdourrahmane.Atto@univ-smb.fr* - Phone: +334 50 09 65 27 - Fax: +334 50 09 65 59

The work was supported by PHOENIX ANR-15-CE23-0012 grant of the French *National Agency of Research.*

Most of these methods yield computationally greedy algorithms because they have been built for the sole sake of performance over short-length image sequences.

For long-time sequences such as those expected with the future Sentinel constellation, a direct application of these methods is not an option: this direct application may be unthinkable due to computational cost and unnecessary for performance/robustness. Indeed, dense/long temporal sampling results in redundant information on the time axis so that a purely temporal analysis may be sufficient for monitoring of most large scale earth structures.

The issue raised by new generation SAR sensors is thus revisiting these methods with the sake of adapting them to long and dense temporal image samples. Among the references provided above, we consider hereafter wavelet based approaches derived in [8], [13] for change detection and in [29],[30] for image regularization.

For change detection, [8] computes a log-ratio change measure and applies a wavelet transform to this log-ratio measure in order to emphasize different levels of changes. In contrast, [13] computes the wavelet transform of images prior to change detection by using probabilistic pixel features.

For image regularization, [29] and [30] propose wavelet shrinkages by using: 1) a parametric Bayesian approach [29] and 2) a non-parametric sigmoid based approach [30]. The wavelet transform applies on the spatial axes for both parametric and non-parametric methods, so as to be more robust to speckle. Despite the somewhat different strategy, parametric and non-parametric approaches can be shown equivalent up to a probabilistic prior specification.

The present paper revisit [8], [13], [29] and [30] for deriving a joint and intuitive framework for change detection and regularization. The main contributions provided by the paper are enumerated through the following paper organization. Section II provides statistical properties of standard (additive) wavelet transforms on a multiplicative observation model. It highlights the non-stationarities of wavelet coefficients when the decomposition applies directly on the multiplicative interactions. A multiplicative wavelet definition from algebraic inference is described in Section III. Its statistical properties on multiplicative observation models are discussed in the same section. This wavelet transform is shown to be associated with stationary and decorrelated noise coefficients when focusing on homogeneous radiometry sections. Section IV provides block sigmoid shrinkage functions for change information enhancement. Section V then exploits both shrinkage and decorrelation induced by the multiplicative wavelets to propose a joint filtering and change detection method for high resolution SAR image time series. Section VI concludes the work.

II. Statistical properties of additive wavelet transforms on multiplicative observation models

A. Problem formulation

A multiplicative observation model involving strictly positive interactions of a piecewise regular deterministic function f and a random process X can be written as:

$$\mathbf{y} = f\mathbf{X} = f + f(\mathbf{X} - 1). \tag{1}$$

In the model given by Eq. (1), function f is observed in a multiplicative signal-independent-noise $\mathbf{X}$ or, equivalently, in an additive signal-dependent-noise $f(\mathbf{X}-1)$. We assume that $\mathbf{X} = (\mathbf{X}[k])_{k\in\mathbb{Z}}$ denotes a stationary sequence of (strictly) positive real random variables.

The (standard) wavelet transform operates on Eq. (1) in a way such that (linearity with respect to '+' operation)

$$\mathcal{W}\mathbf{y} = \mathcal{W}f + \mathcal{W}f(\mathbf{X} - 1). \qquad (\clubsuit)$$

Question: assuming sparsity of $\mathcal{W}$ on f, what are the statistical properties of the noisy observation $\mathcal{W}\mathbf{y}$?

In a noisy environment, the useful sparsity is strongly linked to the noise properties since noise affects the non-zero coefficients, and thus affects the quality of the approximation that can be obtained by considering those non-zero coefficients. Noise being $\mathcal{W}f(\mathbf{X}-1)$ in model $(\clubsuit)$, the issue is then the statistical properties of this quantity.

The following first recalls basics on wavelet transforms (Section II-B). Then Section II-C provides the statistical properties of wavelet coefficients of the noise involved in case $(\clubsuit)$.

B. Basics on wavelet based transforms

In the following, we are interested in multi-scale decomposition schemes involving, up to a normalization constant, some paraunitary filters $(\mathbf{H_0}, \mathbf{H_1})$ associated with a wavelet decomposition, see [31], [32], among other references.

A one-level wavelet decomposition involves splitting a given functional space $\mathbf{W}_{j,n} \subset L^2(\mathbb{R})$, defined as the closure of the space spanned $\{\tau_{2^j k} W_{j,n} : k \in \mathbb{Z}\}$ into direct sums of subspaces $(\mathbf{W}_{j+1,2n+\epsilon})_{\epsilon\in\{0,1\}}$, spanned respectively by $\{\tau_{2^{j+1}k} W_{j+1,2n+\epsilon} : k \in \mathbb{Z}\}_{\epsilon\in\{0,1\}}$, where $\tau_k f : t \longmapsto f(t-k)$. The splitting of $\mathbf{W}_{j,n}$ follows from decimated arithmetic convolution operations:

$$W_{j+1,2n+\epsilon}(t) = \sum_{\ell\in\mathbb{Z}} \mathbf{h}_\epsilon[\ell] W_{j,n}(t - 2\ell). \tag{2}$$

for $\epsilon \in \{0,1\}$, where $\mathbf{h}_\epsilon$ denotes the impulse response of the *scaling filter* (when $\epsilon = 0$) or the wavelet filter (when $\epsilon = 1$).

The consequence of Eq. (2) is that a function g having coefficients $c = (c[\ell])_{\ell\in\mathbb{Z}} \in \ell^2(\mathbb{Z})$ on $\{\tau_{2^j k} W_{j,n} : k \in \mathbb{Z}\}$:

$$g = \sum_{\ell\in\mathbb{Z}} c[\ell] \tau_{2^j \ell} W_{j,n} \in \mathbf{W}_{j,n}$$

can be expanded[1] in terms of

$$g = \underbrace{\sum_{\ell\in\mathbb{Z}} c_0[\ell]\tau_{2^{j+1}\ell}W_{j+1,2n}}_{\in \mathbf{W}_{j+1,2n}} + \underbrace{\sum_{\ell\in\mathbb{Z}} c_1[\ell]\tau_{2^{j+1}\ell}W_{j+1,2n+1}}_{\in \mathbf{W}_{j+1,2n+1}}$$

For $\epsilon \in \{0,1\}$, function g coefficients $c_\epsilon = (c_\epsilon[\ell])_{\ell\in\mathbb{Z}}$ on $\{\tau_{2^{j+1}k}W_{j+1,2n+\epsilon} : k \in \mathbb{Z}\}_{\epsilon\in\{0,1\}}$ satisfy

$$c_\epsilon[k] = \sum_{\ell\in\mathbb{Z}} \mathbf{h}_\epsilon[\ell]c[\ell-2k]. \quad (3)$$

Thus, in practice, starting the decomposition from a function $f \in \mathbf{W}_{0,0}$,

$$f = \sum_{\ell\in\mathbb{Z}} c[\ell]\tau_\ell W_{0,0},$$

the subband $W_{j,n}$ coefficients of f follow from

$$c_{j,n}[k] = \sum_{\ell\in\mathbb{Z}} \mathbf{h}_{j,n}[\ell]c[\ell-2^jk] \quad (4)$$

where the Fourier transform $\mathbf{H}_{j,n}$ of $\mathbf{h}_{j,n}$ is:

$$\mathbf{H}_{j,n}(\omega) = 2^{j/2}\left[\prod_{\ell=1}^{j}\mathbf{H}_{\epsilon_\ell}(2^{\ell-1}\omega)\right]. \quad (5)$$

Eq. (4) can be used in practice for computing discrete wavelet transforms from sample observations (terminologies of 'discrete wavelet transform' when $n \in \{0,1\}$, 'discrete wavelet packet transform' when $n \in \{0,1,\ldots,2^j-1\}$, 'adapted discrete wavelet packets' for a suitable selection of n-indices). Some splitting schemes involving non-decimation (factor 2^j in Eq. (4)) are also available and yield the concept of frames and the notion of stationary wavelet transforms [33]. The reader can refer to the general literature on wavelets for more details on wavelet transforms.

C. Stochasticity properties of the additive wavelet coefficients

In model (♣), noise is associated with a random sequence having the form

$$\mathbf{Y}[k] = f[k](\mathbf{X}[k]-1). \quad (6)$$

Since we have assumed that $(\mathbf{X}[k])_{k\in\mathbb{Z}}$ are stationary, say $\mathbb{E}\mathbf{X}[k] = \mu_0$ and autocorrelation function $R_{\mathbf{X}}[k,\ell] = \mathbb{E}[\mathbf{X}[k]\mathbf{X}[\ell]] \triangleq R_{\mathbf{X}}[k-\ell]$, then:

- The mean of $\mathbf{Y}[k]$ is

$$\mathbb{E}\mathbf{Y}[k] = f[k](\mu_0-1). \quad (7)$$

- The autocorrelation function of $\mathbf{Y}$, $R_{\mathbf{Y}}[k,\ell] = \mathbb{E}[\mathbf{Y}[k]\mathbf{Y}[\ell]]$ satisfies, by taking into account Eq. (6):

$$R_{\mathbf{Y}}[k,\ell] = f[k]f[\ell]\,(R_{\mathbf{X}}[k-\ell]-1). \quad (8)$$

[1] Equalities hold true in $L^2(\mathbb{R})$ sense in these expansions.

Remark 1: Eqs. (7) and (8) above highlight that the additive signal-dependent noise $\mathbf{Y}$ is non-stationary in general, except in some very few cases, for instance when f is constant.

Let us now analyze the wavelet coefficients of $\mathbf{Y}$. Denote by $\mathbf{C}^+_{j,n}$ the coefficients of $\mathbf{Y}$ on subband $\mathbf{W}_{j,n}$. We have

$$\mathbf{C}^+_{j,n}[k] = \sum_{\ell\in\mathbb{Z}} \mathbf{h}_{j,n}[\ell]f[\ell-2^jk](\mathbf{X}[\ell-2^jk]-1). \quad (9)$$

It follows that

$$\mathbb{E}\mathbf{C}^+_{j,n}[k] = (\mu_0-1)\sum_{\ell\in\mathbb{Z}} \mathbf{h}_{j,n}[\ell]f[\ell-2^jk] \quad (10)$$

and the autocorrelation function $R^+_{j,n}[k,\ell] = \mathbb{E}\left[\mathbf{C}^+_{j,n}[k]\mathbf{C}^+_{j,n}[\ell]\right]$ of $\mathbf{C}^+_{j,n}$ is:

$$R^+_{j,n}[k,\ell] = \sum_{p\in\mathbb{Z}}\sum_{q\in\mathbb{Z}} \mathbf{h}_{j,n}[p]h_{j,n}[q]\times f[p-2^jk]f[q-2^j\ell]\times \left(R_{\mathbf{X}}[p-q-2^j(k-\ell)]-1\right). \quad (11)$$

From Eq. (11), we derive that $\mathbf{C}^+_{j,n}$ is non-stationary in general due to the presence of the term $f[p-2^jk]f[q-2^j\ell]$ in Eq. (11) and this, even if $\mu_0 = 1$ in Eq. (10).

Remark 2 (Non-stationarity of $\mathbf{C}^+_{j,n}$ for exponential type function f): Assume that $\mu_0 = 1$ and function f satisfies $f[k]f[\ell] = f[k+\ell]$ (exponential type functions), where f does not reduce to the constant 1. In this case, we derive

$$R^+_{j,n}[k,\ell] = \frac{f[-2^j(k+\ell)]}{2\pi}\times \left(\int_{-\pi}^{\pi}\gamma_{\mathbf{X}^0}(\omega)\,|G_{j,n}(\omega)|^2\,e^{i2^j(k-\ell)\omega}\,d\omega\right) \quad (12)$$

where $G_{j,n} = F * \mathbf{H}_{j,n}$ and F is the Fourier transform of f. The non-stationarity of $C^+_{j,n}$ is then due to the term $f[-2^j(k+\ell)]$ in Eq. (12) above.

More generally, even when assuming that $\mu_0 = 1$, it is easy to check that most standard functions f lead to the non-stationarity of $C^+_{j,n}$. In particular, linear functions of type $f[k] = f_0 \times k$ (for certain k in a finite set) have a term in $k\ell$ which cannot be reduced as a function of the single variable $m = k-\ell$. High order polynomial functions have bivariate monomial terms involving $k^\lambda\ell^\eta$ in $R^+_{j,n}[k,\ell]$. Functions of type sin, cos satisfy $f[k]f[\ell] = g_1[k+\ell]+g_2[k-\ell]$ and in this case, the contribution of g_1 implies non-stationarity as in the exponential case given above, *etc.*

An appealing case of a stationary sequence $\mathbf{C}^+_{j,n}$ corresponds to a constant function f associated with a random sequence $\mathbf{X}$ with unit mean:

Remark 3 (Stationarity): When $\mu_0 = 1$ and f is a constant function: $f[k] = f_0$, then $\mathbb{E}\mathbf{C}^+_{j,n}[k] = 0$ and

furthermore, we derive $R^+_{j,n}[k,\ell] = R^+_{j,n}[k-\ell] = R^+_{j,n}[m]$ with:

$$R^+_{j,n}[m] = \frac{f_0^2}{2\pi}\int_{-\pi}^{\pi} \gamma_{\mathbf{X}^0}(\omega)\,|\mathbf{H}_{j,n}(\omega)|^2\, e^{i2^j m\omega}\,d\omega \quad (13)$$

where $\gamma_{\mathbf{X}^0}$ denotes the spectrum of the random sequence $\mathbf{X}^0 = \mathbf{X} - 1$.

$$\gamma_{\mathbf{X}^0}(\omega) = \sum_{m\in\mathbb{Z}} (R_{\mathbf{X}}[m] - 1)\, e^{-im\omega}.$$

This case of a constant function f observed in a multiplicative noise represents homogeneous area observation in practical SAR applications. This case is the sole favorable scenario for stationarity of standard additive wavelet details when noise is multiplicative as in model $f\mathbf{X}$.

Due to the non-stationarity of $\mathbf{C}^+_{j,n}$ in general (except few cases such as that of Remark 3), modeling or estimating additive wavelet coefficients of a multiplicative model is not an easy task. The following shows that multiplicative implementations of wavelets highlight desirable stochasticity properties for simplifying model $f\mathbf{X}$.

III. Multiplicative wavelet implementation - Statistical properties on multiplicative observation models

A multiplicative wavelet transform (multiplicative linearity where $\mathcal{W}$ distributes over '$\times$' operation), when applied on model given by Eq. (1), must satisfy:

$$\mathcal{W}\mathbf{y} = (\mathcal{W}f) \times (\mathcal{W}\mathbf{X}). \qquad (\spadesuit)$$

This transform is derived hereafter from multiplicative convolution operator.

Note that performing a geometric wavelet decomposition satisfying model ($\spadesuit$) amounts to apply a log-transform on the input data, perform a standard wavelet transform and apply an exponential transform on the wavelet coefficients of this standard transform. We consider hereafter the description of such operations by directly embedding wavelet operators in a multiplicative algebra with *binary internal multiplication* and *external power operation*.

A. Multiplicative (geometric) convolution

The binary operation considered in the following is the multiplication ($\times$ symbol) over positive real numbers $\mathbb{R}^+$.

Consider a data sequence $\mathbf{x} = (\mathbf{x}[\ell])_{\ell\in\mathbb{Z}}$, with $\mathbf{x}[\ell] \in \mathbb{R}^+$ for every $\ell \in \mathbb{Z}$. Since this sequence represents a multiplicative phenomenon, then

- "zero" or "nothing" or "no change" corresponds to the identity element "1"
- a "small" value is a value close to 1 (10^{-3} and 10^3 have the same significance in terms of *absolute proportion*,
- a missing value must be replaced by 1,
- shrinkage forces to 1, the coefficients that are close to 1.

The multiplicative algebra implies defining the support of the sequence $\mathbf{x}$ as the sub-sequence composed with elements that are different from 1. We will thus use the standard terminologies of finite/infinite supports with respect to the above remark. When such a sequence $\mathbf{x}$ is infinite, we will assume that $\log(\mathbf{x}) = ((\log \mathbf{x}[k])_{k\in\mathbb{Z}}) \in \ell^2(\mathbb{Z})$.

When considering a scalar sequence (impulse response of a filter for instance) $\mathbf{h} = (\mathbf{h}[\ell])_{\ell\in\mathbb{Z}}$ where $\mathbf{h}[\ell] \in \mathbb{R}$ for every $\ell \in \mathbb{Z}$, then we will keep the standard terminology related to support definition from non-zero elements (non-null real numbers).

The multiplicative convolution defined below is based on this binary operation (notation $x \times y \triangleq xy$ for $x, y \in \mathbb{R}^+$) and real scalar power operations (notation $a \wedge x \triangleq x^a$ for $x \in \mathbb{R}^+$ and $a \in \mathbb{R}$).

Definition 1 (Multiplicative convolution): Let $\mathbf{h} = (\mathbf{h}[\ell])_{\ell\in\mathbb{Z}}$ denote the impulse response of a digital filter. We define the multiplicative convolution of $\mathbf{x}$ and $\mathbf{h}$ on $(\mathbb{R}^+, \times, \wedge)$ as:

$$\begin{aligned}\mathbf{y}[k] = \mathbf{x} \circledast \mathbf{h}[k] &\triangleq \prod_{\ell\in\mathbb{Z}} (\mathbf{x}[\ell])^{\mathbf{h}[k-\ell]} \\ &= \prod_{\ell\in\mathbb{Z}} (\mathbf{x}[k-\ell])^{\mathbf{h}[\ell]} \triangleq \mathbf{h} \circledast \mathbf{x}[k]. \quad (14)\end{aligned}$$

One can remark that, in contrast to the standard convolution operation on $(\mathbb{R}, +, \times)$ sequences, discrete sequence $\mathbf{h}$ plays here a non-commutative scalar role with respect to $\mathbf{x}$ since the external operation 'power' used in Eq. (14) is not commutative. This justifies the second $\triangleq$ in Eq. (14): the equality $\mathbf{x} \circledast \mathbf{h} = \mathbf{h} \circledast \mathbf{x}$ applies index-wise on the multiplicative convolution, given that the scalar sequence $\mathbf{h}$ operates to the power of elements of $\mathbf{x}$, by definition.

If $\mathbf{h} \in \ell^2(\mathbb{Z})$, then $\mathbf{x} \circledast \mathbf{h}[k]$ exists and is finite for almost every k since we have assumed that $\log(\mathbf{x}) \in \ell^2(\mathbb{Z})$. Depending on $\mathbf{h}$, Eq. (14) makes the computation of multiplicative approximations and details of the input data $\mathbf{x}$ possible.

An example of multiplicative approximation is obtained by the so-called *geometric mean* of a finite sequence $\{x_1, x_2, \ldots, x_N\}$:

$$y = \sqrt[N]{x_1 x_2 \cdots x_N} = \prod_{\ell=1}^{N} x_\ell^{1/N}. \quad (15)$$

This geometric mean is associated with an N-length Haar-type approximation filter

$$\mathbf{h_0}[k] = \nu \;\text{ for }\; k = 1, 2, \ldots, N. \quad (16)$$

Multiplicative approximations computed by using the filter $\mathbf{h_0}$ (*low pass filter*) will thus be called *geometric approximations*. Filter $\mathbf{h_0}$ can be associated with a Haar-type detail filter:

$$\mathbf{h_1}[k] = (-1)^{k-1}\nu \text{ for every } k = 1, 2, \ldots, N \quad (17)$$

which performs *geometric differencing* (ratio involving several consecutive elements), where constant $\nu > 0$ is fixed so as to impose paraunitarity for the corresponding pair of filters ($\nu = \sqrt{2}/2$ for standard **Haar** wavelet filters when $N = 2$). For the sake of standardizing terminology, the multiplicative convolution of Eq. (14) will be called *geometric convolution* whatever the filter used and the same holds true for the wavelet transform defined below.

B. Multiplicative (geometric) wavelet decomposition

In the following, we consider the same paraunitary *wavelet filters* $(\mathbf{h}_0, \mathbf{h}_1) \in \ell^2(\mathbb{Z}) \times \ell^2(\mathbb{Z})$ as in Section II-B. Let

$$\overline{\mathbf{h}[k]} = \mathbf{h}[-k].$$

Define the wavelet decomposition of $\mathbf{x}$ with respect to the geometric convolution (*geometric wavelet decomposition*) by:

$$\mathbf{c}_{1,0}[k] = \mathbf{x} \circledast \overline{\mathbf{h}_0}[2k], \quad (18)$$

$$\mathbf{c}_{1,1}[k] = \mathbf{x} \circledast \overline{\mathbf{h}_1}[2k] \quad (19)$$

and, recursively, for $\epsilon \in \{0, 1\}$ (wavelet packet splitting formalism described in [32]):

$$\mathbf{c}_{j+1,2n+\epsilon}[k] = \mathbf{c}_{j,n} \circledast \overline{\mathbf{h}_\epsilon}[2k]. \quad (20)$$

In the decomposition given by Eq. (20) above, sequence $\mathbf{c}_{j+1,2n+\epsilon}$ represents:

- geometric approximation of $\mathbf{c}_{j,n}$ when $\epsilon = 0$,
- geometric differencing (ratio details) of $\mathbf{c}_{j,n}$ when $\epsilon = 1$.

The level $j = 0$ coefficients represent the input sequence $\mathbf{x}$. As in the standard case, the above wavelet packet splitting is associated to a wavelet decomposition when subspace splitting concerns only approximations $(\mathbf{c}_{j,0})_{j \geqslant 1}$.

***Proposition** 1 (Geometric wavelet reconstruction):* We have:

$$\mathbf{c}_{j,n}[k] = (\check{\mathbf{c}}_{j+1,2n} \circledast \mathbf{h}_0[k]) \times (\check{\mathbf{c}}_{j+1,2n+1} \circledast \mathbf{h}_1[k]), \quad (21)$$

where

$$\check{\mathbf{u}}[2k + \epsilon] = \begin{cases} \mathbf{u}[k] & \text{if } \epsilon = 0, \\ 1 & \text{if } \epsilon = 1. \end{cases} \quad (22)$$

Proof: The proof is a direct consequence of the expansion of the right hand side of Eq. (21), by taking into account Eq. (20) and the paraunitary condition which imposes $\sum_{\ell \in \mathbb{Z}} \mathbf{h}_\epsilon[\ell]\overline{\mathbf{h}_\epsilon}[\ell - 2k] = \delta[k]$. ■

Proposition 1 represents the reconstruction of the level-j-wavelet-coefficients from the coefficients located at level $j + 1$. As in the standard additive formulation given in Section II-B (see Eq. (3)), different wavelet decomposition schemes (orthogonal wavelets, stationary wavelets, adapted wavelet packets, *etc.*) and perfect reconstructions can be obtained from Eqs. (20) and (21) respectively.

This geometric transform is nothing but the formalization of "log transform of data before wavelets and exp transform of coefficients after wavelets" in terms of an algebraic inference where implementation implies

- executing environment $(\times, \wedge)$ for every call of environment $(+, \times)$ and
- replacing calls of '0s' by '1s' (decimation corresponds to replacing one coefficient out of two by the number 1).

In the following, we will address the statistical properties of the coefficients issued from Eq. (20).

C. Statistical properties of the geometric wavelet transform on Eq. (1)

The geometric wavelet decomposition $\mathcal{W}^\times$ of Eq. (20) distributes over the product $f\mathbf{X}$: $\mathcal{W}^\times[f\mathbf{X}] = (\mathcal{W}^\times f)(\mathcal{W}^\times \mathbf{X})$. Thus, in model (♠), with $\mathcal{W} = \mathcal{W}^\times$ defined by Eq. (20), noise contribution is $\mathcal{W}^\times\mathbf{X}$ where we have assumed that $\mathbf{X} = (\mathbf{X}[k])_{k \in \mathbb{Z}}$ is a stationary unit-mean random sequence. Assuming sparsity of $\mathcal{W}^\times$ on f, the focus of this section is establishing the statistical properties of $\mathcal{W}^\times\mathbf{X}$.

The geometric wavelet coefficients of the decomposition of $\mathbf{X}$ on subspace $\mathbf{W}_{j,n}$ will be denoted $(\mathbf{C}^\times_{j,n})_{j,n}$ (we assume that this stochastic sequence is well defined in the following). Note that if $\mathbf{C}_{j+1,2n+\epsilon}[k] = \mathbf{C}_{j,n} \circledast \overline{\mathbf{h}_\epsilon}[2k]$ where $\mathbf{C}_{j,n}$ is a stationary sequence, then $\mathbf{C}_{j+1,2n+\epsilon}$ is also stationary. Since $\mathbf{C}_{0,0} = \mathbf{X}$ is assumed to be stationary, we derive that all geometric wavelet sequences $\mathbf{C}_{j,n}$ are stationary for $j \geqslant 0$ and $n \in \{0, 1, \ldots, 2^j - 1\}$.

Let $\mathbf{Y} = \log \mathbf{X}$. We assume hereafter that $\mathbf{Y}$ is a second-order random process, continuous in quadratic mean. Let $\mathbf{D}_{j,n} = \log \mathbf{C}^\times_{j,n}$. Note that $\mathbf{Y}$ and $\mathbf{D}_{j,n}$ are stationary sequences. Assume that $\mathbb{E}\mathbf{Y}[k] = 0$ for every $k \in \mathbb{Z}$. Then $\mathbb{E}\mathbf{D}_{j,n}[k] = 0$ for every $k \in \mathbb{Z}$.

Let $R_{\mathbf{Y}}[m] = R_{\mathbf{Y}}[k-\ell] = \mathbb{E}[\mathbf{Y}[k]\mathbf{Y}[\ell]]$ be the autocorrelation function of $\mathbf{Y}$, where the first equality above holds true for any pair $(k, \ell) \in \mathbb{Z} \times \mathbb{Z}$ such that $m = \pm|k - \ell|$. Proposition 2 below derives the autocorrelation function $R_{\mathbf{D}_{j,n}}$ of the log-scaled geometric wavelet coefficient $\mathbf{D}_{j,n}$. We assume that $\sum_{q \in \mathbb{Z}} \mathbf{h}_\epsilon[p - 2k]\mathbf{h}_\epsilon[q - 2\ell]R_{\mathbf{D}_{j,n}}[p, q]$ exists for every $j \geqslant 0$ and $n \in \{0, 1, \ldots, 2^j - 1\}$.

***Proposition** 2 (Autocorrelation Function of $\mathbf{D}_{j,n}$):* Assume that $R_{\mathbf{Y}}$ has a spectrum (power spectral density)

$$\gamma_{\mathbf{Y}}(\omega) = \sum_{m \in \mathbb{Z}} R_{\mathbf{Y}}[m]e^{-im\omega}$$

and that $\gamma_{\mathbf{Y}}$ is bounded. Denote by $\gamma_{\mathbf{D}_{j,n}}$, the spectrum of $\mathbf{D}_{j,n}$:

$$\gamma_{\mathbf{D}_{j,n}}(\omega) = \sum_{m\in\mathbb{Z}} R_{\mathbf{D}_{j,n}}[m]e^{-im\omega}. \quad (23)$$

We have, for $j \geqslant 0$, $n \in \{0,1,\ldots,2^{j-1}\}$ and $\epsilon \in \{0,1\}$:

$$R_{\mathbf{D}_{j+1,2n+\epsilon}}[m] = \frac{1}{2\pi}\int_{-\pi}^{\pi}\left|\widehat{\mathbf{H}_\epsilon}(\omega)\right|^2 \gamma_{\mathbf{D}_{j,n}}(\omega)e^{2im\omega}d\omega, \quad (24)$$

where $\gamma_{\mathbf{D}_{0,0}} = \gamma_{\mathbf{Y}}$.

Proof: See Appendix A. ∎

By taking into account that sequence $\mathbf{D}_{j,n}$ issues from a filter bank $(H_{\epsilon_\ell})_{\ell=1,2,\ldots,j}$ (low-pass when $\epsilon_\ell = 0$ and high-pass when $\epsilon_\ell = 1$) and has the equivalent representation given by Eq. (5), we derive recursively from Eq. (24):

$$R_{\mathbf{D}_{j,n}}[m] = \frac{1}{2\pi}\int_{-\pi}^{\pi} |\mathbf{H}_{j,n}(\omega)|^2 \gamma_{\mathbf{Y}}(\omega)e^{2^j im\omega}\, d\omega. \quad (25)$$

Eq. (25) governs the behavior of the autocorrelation of $\mathbf{D}_{j,n}$. From this equation, decorrelating geometric wavelet coefficients involves selecting wavelet filters such that quantity

$$\frac{1}{2\pi}\int_{-\pi}^{\pi} |\mathbf{H}_{j,n}(\omega)|^2 \gamma_{\mathbf{Y}}(\omega)\cos 2^j m\omega\, d\omega \quad (26)$$

behaves approximately like Dirac $\delta[m]$. This is strongly linked to the shape of $\gamma_{\mathbf{Y}}$ and can be achieved either by:

(i) choosing a sequence of wavelet filters such that function $|\mathbf{H}_{j,n}(\omega)|^2\gamma_{\mathbf{Y}}(\omega)$ is approximately constant or
(ii) seeking asymptotic decorrelation with j (provided that it applies).

Item (i) is parametric in the sense that it relates to adapted wavelet selection for decorrelating $\mathbf{Y}$. Item (ii) (non-parametric) exploits properties of recursive convolutions. For instance, if we consider the Haar wavelet filters (used below for illustrations), we can derive:

***Proposition** 3 (Haar equivalent wavelet filter sequence $\mathbf{H}_{j,n}^{Haar}$):* A sequence $(\mathbf{h}_{\epsilon_\ell})_{\ell=1,2,\ldots,j}$ has equivalent filter:

$$\left|\mathbf{H}_{j,n}^{\text{Haar}}(\omega)\right|^2 = 2^j\prod_{\ell=1}^{j}\cos^2\left(2^{\ell-2}\omega + \epsilon_\ell\frac{\pi}{2}\right). \quad (27)$$

Proof: See Appendix B. ∎

In the usual wavelet splitting scheme, only approximation coefficients are decomposed again (the shift parameter $n \in \{0,1\}$). This implies filtering sequences with the form

$$\left(\underbrace{\mathbf{h}_0,\mathbf{h}_0,\ldots,\mathbf{h}_0}_{j\text{ times}},\mathbf{h}_{\epsilon_{j+1}}\right)_{\epsilon_{j+1}\in\{0,1\}}$$

at decomposition level $j+1$. Consider a j-length approximation sequence $\left(\mathbf{h}_0^{\text{Haar}}\right)_{\ell=1,2,\ldots,j}$ of Haar type. Then from Eq. (27), the equivalent filter of this sequence can be rewritten in the form:

$$\left|\mathbf{H}_{j,0}^{\text{Haar}}(\omega)\right|^2 = 2^j\left(\frac{\text{sinc}(2^{j-1}\omega)}{\text{sinc}(2^{-1}\omega)}\right)^2, \quad (28)$$

where sinc denotes the *cardinal sine* function, $\text{sinc}\omega = \sin\omega/\omega$. The autocorrelation $R_{\mathbf{D}_{j,0}}^{\text{Haar}}$ of the corresponding geometric wavelet coefficients is then:

$$R_{\mathbf{D}_{j,0}}^{\text{Haar}}[m] = \frac{2^j}{\pi}\int_0^{\pi}\left(\frac{\text{sinc}(2^{j-1}\omega)}{\text{sinc}(2^{-1}\omega)}\right)^2\gamma_{\mathbf{Y}}(\omega)\cos 2^j m\omega\, d\omega. \quad (29)$$

***Proposition** 4 (Limit Autocorrelation Function):*

$$\lim_{j\to+\infty} R_{\mathbf{D}_{j,0}}^{\text{Haar}}[m] = \gamma_{\mathbf{Y}}(0)\delta[m] \quad (30)$$

Proof: See Appendix C. ∎

Proposition 4 highlights an asymptotic decorrelation property with j. This property can be extended by considering different paraunitary filters. For instance, when considering the N-*length Haar-type* approximation filter $\mathbf{h_0}$ and detail filter $\mathbf{h_1}$ given by Eqs. (16) and (17), the equivalent wavelet filter is

$$|\mathbf{H}_{j,n}(\omega)|^2 = 2^j\prod_{\ell=1}^{j}\left(\frac{\sin(2^{\ell-2}N\omega)}{\sin(2^{-1}(\omega+\epsilon_\ell\pi))}\right)^2. \quad (31)$$

It follows that the corresponding autocorrelation $R_{\mathbf{D}_{j,n}}$ is

$$\begin{aligned} &R_{\mathbf{D}_{j,n}}[m] \\ &= \frac{2^j}{\pi}\int_0^{\pi}\prod_{\ell=1}^{j}\left(\frac{\sin(2^{\ell-2}N\omega)}{\sin(2^{-1}(\omega+\epsilon_\ell\pi))}\right)^2\gamma_{\mathbf{Y}}(\omega)\cos 2^j m\omega\, d\omega, \\ &= \frac{1}{\pi}\int_0^{\pi}\prod_{\ell=1}^{j}\left(\frac{\sin(2^{-j+\ell-2}N\omega)}{\sin(2^{-j-1}\omega+\epsilon_\ell\frac{\pi}{2})}\right)^2\gamma_{\mathbf{Y}}\left(\frac{\omega}{2^j}\right)\cos m\omega\, d\omega \end{aligned}$$

which tends to $\gamma_{\mathbf{Y}}(0)\delta[m]$ when j tends to ininity, for the approximation path ($n = 0$).

This decorrelation property can also be extended by considering different paths, filters and wavelet packet splitting schemes, as done in [34] for additive noise and arithmetic wavelet transforms.

IV. Change detection: parsimony of the signal-versus-noise separation makes relevant basic dissimilarity operators

A. Change information perceived from arithmetic and geometric differencing

From now on, we will use the terminologies of discrete *Arithmetic Wavelet Transform* (AWT) and *Geometric Wavelet Transform* (GWT) to point out, respectively, the additive and multiplicative implementations given by Eq. (4) and Eq. (20).

When analyzing the multiplicative interactions in observation $\mathbf{y}$ given by Eq. (1), Section II has shown that AWT coefficients will be non-stationary in general whereas

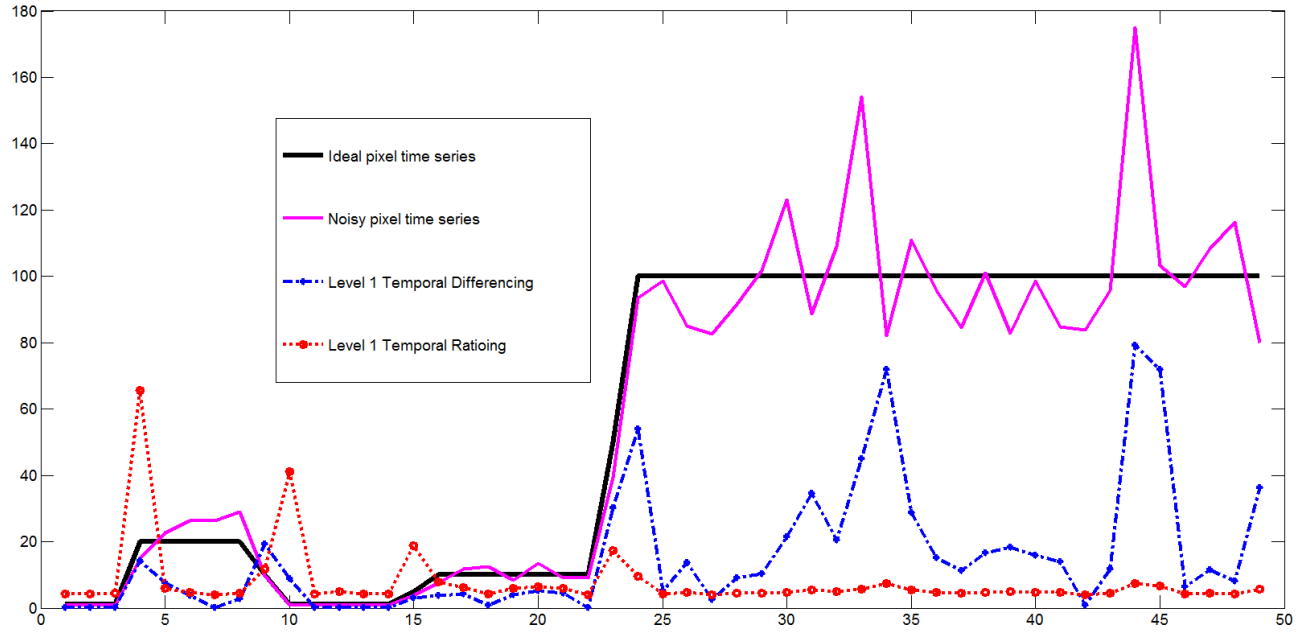

Fig. 1. Pixel time series with 4 change dates, its noisy speckled version, as well as absolute change information from arithmetic differencing (corresponds to Haar level-1 AWT details) and ratioing (geometric differencing, corresponds to Haar level-1 non sub-sampled GWT details). The ratio-data have been re-scaled logarithmically so as to make comparison on a single display possible.

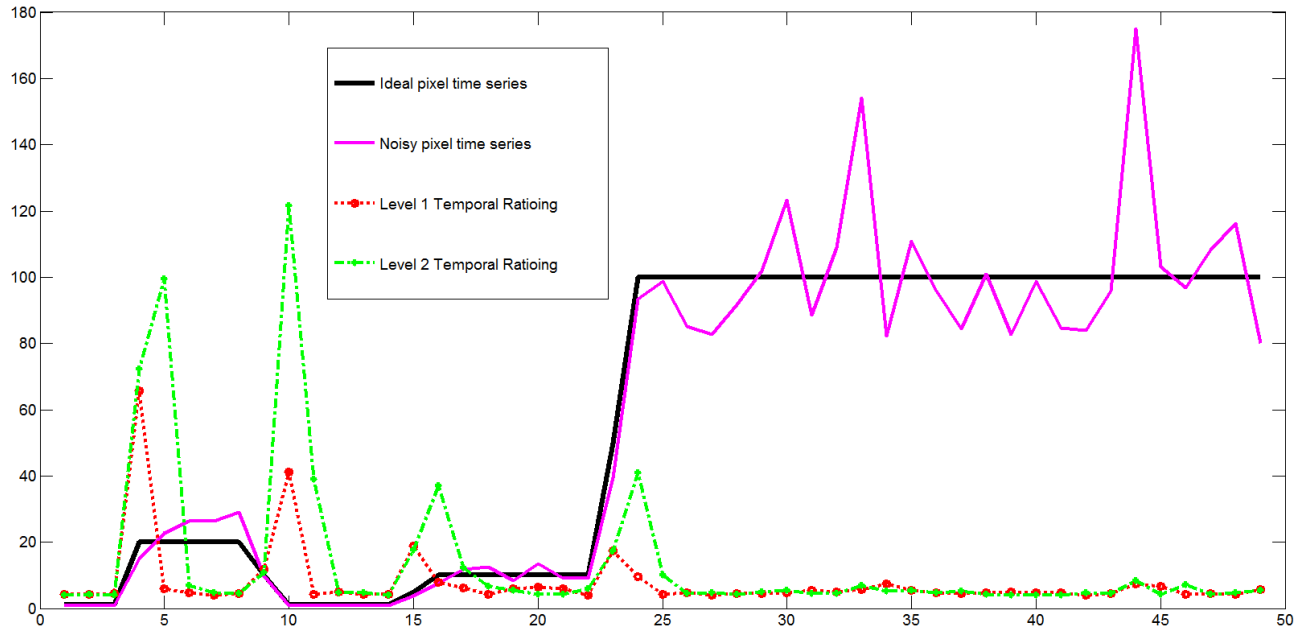

Fig. 2. Pixel time series with 4 change dates, its noisy speckled version, as well as absolute level 1 and 2 ratioing (non sub-sampled GWT). The ratio-data have been re-scaled logarithmically.

GWT coefficients are stationary and, in addition, GWT has a noise decorrelation property (see Section III).

Let us consider the level $j = 1$ details obtained by using Haar filters with $N = 2$ in Eq. (17) (one vanishing moment wavelet). These details are proportional to:

- $y_k - y_{k-1}$ for AWT (*arithmetic differencing* of $(\mathbb{R}, +)$ elements),
- y_k / y_{k-1} for GWT (*geometric differencing* $\Rightarrow$ *ratioing* of $(\mathbb{R}^+, \times)$ elements).

These *differencing operators* are the basic ones used in change evaluation. The 'main difference' between these basic arithmetic and the geometric differencing operators on the observation model of Eq. (1) is illustrated in Figure 1.

As it can be seen in Figure 1, change information can be retrieved without effort with the basic geometric differencing (sparsity of change information, in addition with noise decorrelation) whereas a non-intuitive post-

processing needs to be performed for observing the same changes for the arithmetic differencing, due to strong correlations induced by $f(\mathbf{X}-1)$. Some examples of level-1 generalized wavelet based ratioing (geometric wavelet differencing) are given below.

- Case of a biorthogonal wavelet with 2 vanishing moments:
$$\frac{y_{k-1}^{0.35}y_{k+1}^{0.35}}{y_k^{0.70}}. \tag{32}$$
- Case of a box spline wavelet with 2 vanishing moments:
$$\frac{y_{k-1}^{0.6875}y_{k-2}^{0.21875}y_{k-3}^{0.03125}}{y_k^{0.6875}y_{k+1}^{0.21875}y_{k+2}^{0.03125}}. \tag{33}$$

Depending on the sharpness of the change transitions, it might be relevant to consider multi-level changes. For instance, the transitions between temporal observations of Figure 1 being linear (non-instantaneous), level $j=2$ Haar geometric details are shown to discriminate well change transitions of this observation in Figure 2.

In the rest of the paper, we consider only the geometric wavelet framework for a straightforward change enhancement (sparsity of the geometric temporal details in decorrelated noise).

B. Sigmoid enhancement of change information

Consider the synthetic image time series $\mathcal{P} = (\mathcal{P}_{m,q}(t_k))_{k=1,2,3,4}$ given by Figure 3-[Row 1], where m, q ($1 \leqslant m, q \leqslant 2048$) refer to spatial variables and t_k denotes the time variable. Figure 3-[Row 2] provides change information (binary masks) between the different dates, with $\mathcal{M}(t_k, t_{k+1})$ denoting changes in-between dates t_k and t_{k+1} and $\mathcal{M}^\circ(t_1, t_2, t_3, t_4)$ the total amount of changes.

When applying a geometric wavelet transform $\mathcal{W}^\times[\mathcal{P}_{m,q}(\bullet)]$ with respect to the time axis solely (in practice, this assumes an accurate image registration), then the detail subbands[2] $\left(\mathbf{C}^\times_{j,n}[\mathcal{P}_{m,q}](\bullet)\right)_{1\leqslant m,q\leqslant 2048}$ displayed as images in Figure 3-[Row 3] provide spatio-temporal multiscale change information. These subbands are hereafter called *change-images*. As expected (consequence of Section III), these spatio-temporal geometric change-images show both sparsity of change information (changes are rare and significant when present) and stationarity/decorrelation for speckle noise in homogeneous areas with no temporal change information.

The change enhancement proposed below involves using a spatio-temporal block shrinkage for smoothly penalizing weak changes in pixel intensities. This shrinkage will apply through *sigmoid shrinkage* functions [30]. These functions have the following form:

$$\delta_{\tau,\theta,\lambda}(x) = \frac{\operatorname{sgn}(x)(|x|-\tau)_+}{\left(1+e^{-\zeta(\theta)\left(\frac{|x|}{\lambda}-1\right)}\right)}, \tag{34}$$

where

$$\zeta(\theta) = \frac{10\sin\theta}{2\cos\theta-\sin\theta} \tag{35}$$

with $\operatorname{sgn}(x) = 1$ (resp. -1) if $x \geqslant 0$ (resp. $x < 0$) and, $(x)_+ = x$ (resp. 0) if $x \geqslant 0$ (resp. $x < 0$).

Note that since the wavelet transform is performed with respect to the time axis, a geometric wavelet based-change-image contains:

- either a bidate change information (level $j=1$ detail coefficients when using a filter $\mathbf{h}$ with 2 non-zero coefficients such as Haar filters)
- or a multi-date change information when:
  - $j \geqslant 2$, whatever the filter used, provided that the filter has at least 2 non-zero coefficients,
  - $j \geqslant 1$, when the filter used has more than 2 non-zero coefficients (see for instance Eqs. (32) and (33)).

For highlighting the multi-temporal changes in their spatio-temporal context, the above **sigmoid shrinkage function will be applied hereafter on spatial change-image blocks of *wavelet based temporally differenced data***. For a pixel intensity $Z_{m,q}(k)$ pertaining to a log-scaled change-image, the shrinkage proposed is defined as:

$$\delta_{\tau,\theta,\lambda}(Z_{m,q}(k)) = \frac{\operatorname{sgn}(Z_{m,q}(k))(|Z_{m,q}(k)|-\tau)_+}{1+e^{-\zeta(\theta)\left(\frac{\|V_{Z_{m,q}(k)}\|_2}{\lambda}-1\right)}} \tag{36}$$

where $V_{Z_{m,q}(k)}$ is a vector with the form $V_{Z_{m,q}(k)} = \{Z_{m,q}(k), m = m-\epsilon_0, \ldots, m+\epsilon_0, q = q-\nu_0, \ldots, q+q_0\}$ and ϵ_0, ν_0 are natural numbers chosen sufficiently small (spatial neighborhood of the detail pixel $(Z_{m,q}(k))$, with $\|\cdot\|_2$ denoting the ℓ^2 norm. This penalized shrinkage then consists in:

- forcing to zero all temporal log-scaled geometric wavelet change-image pixel with spatial neighborhood norm smaller than the first threshold τ,
- attenuating temporal log-scaled geometric wavelet change-image pixel with large spatial neighborhood norm thanks to an attenuation degree θ and a second threshold λ.

Change information processing is thus spatio-temporal due to the presence of variable k (geometric temporal change-image) and the variations of spatial variables m, q.

C. Quantitative change evaluation

In [8], changes are analyzed by shrinking arithmetic wavelet coefficients of (standard) log-ratio images (we

[2]Since $J=2$ for this example, we have, in an orthogonal GWT, 3 multiscale subbands due to decimation steps (2 subbands at level $j=1$ and 1 subband at level $j=J=2$). However, we consider displaying all subbands (no decimation) excepted the border ones in order to highlight different change information.

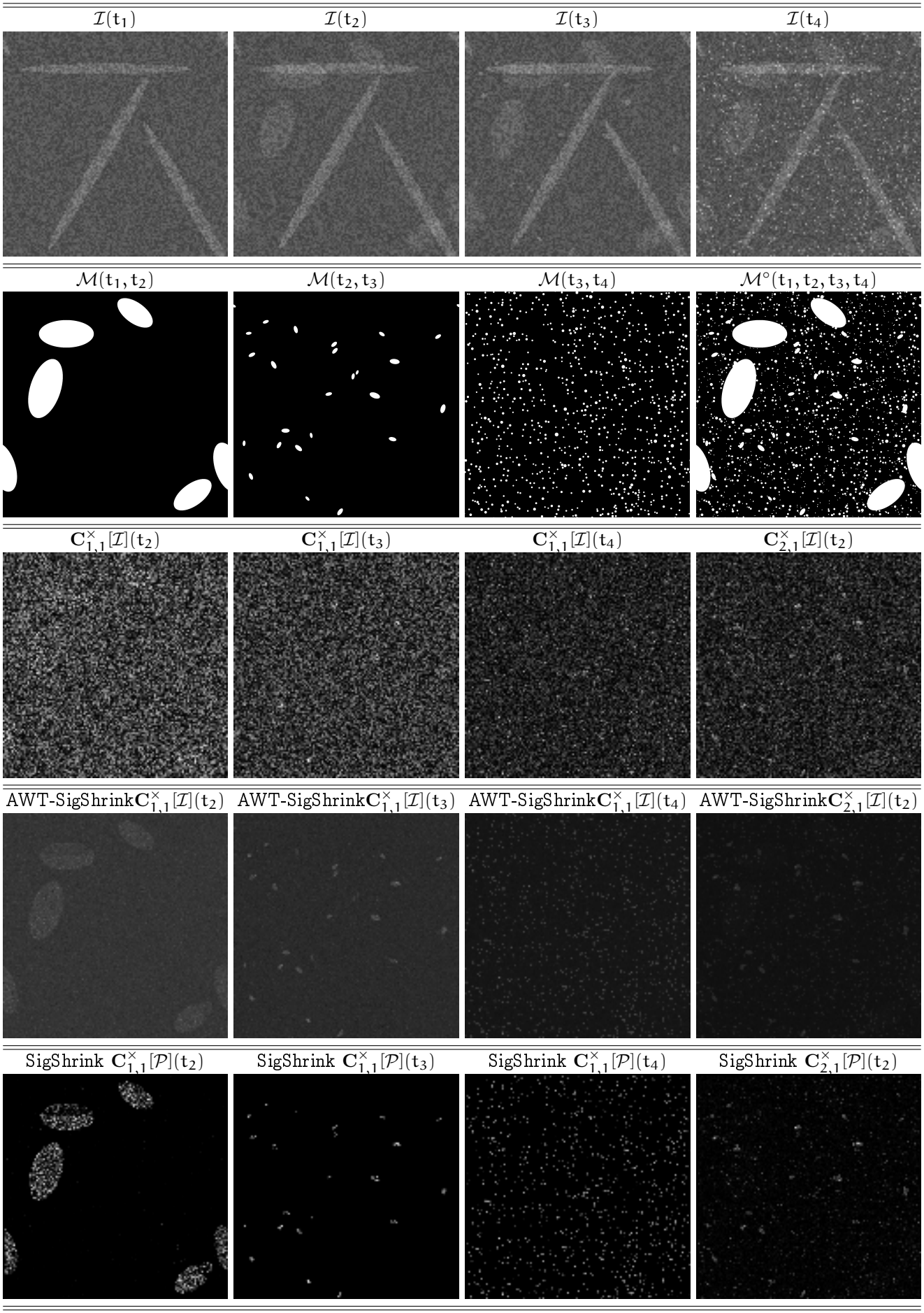

Fig. 3. Row 1: large, small and tiny elliptical structures with different shapes and overlaps, observed in synthetic speckle noise. Row 2: the binary date-to-date and the total $\mathcal{M}^{\circ}$ change maps (true changes). Row 3: Geometric wavelet change-images of time series given in Row 1. Row 4: [AWT-SigShrink] arithmetic wavelet based sigmoid shrinkage (for the geometric change-images given in Row 3). Row 5: [SigShrink] direct block sigmoid shrinkage from Eq. (36) (without additional arithmetic wavelet transform) for the change-images given in Row 3.

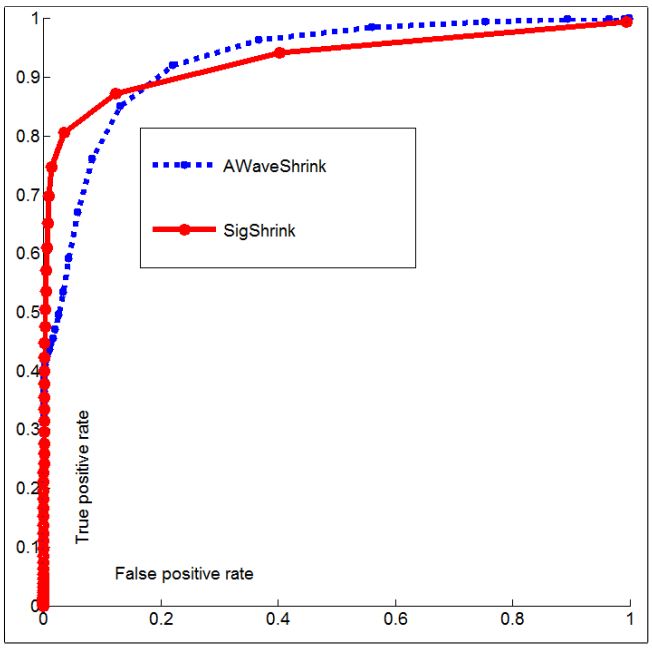

Fig. 4. ROC curves for: 1) AWT-SigShrink (arithmetic wavelet sigmoid shrinkage) of geometric wavelet details and 2) SigShrink (block sigmoid shrinkage of geometric wavelet details). The ROC curves have been computed on the total amount of changes $\mathcal{M}^{\circ}(t_1, t_2, t_3, t_4)$ occurring in the time series of images given by Figure 3.

recall that, from the formalism presented in this paper, the standard log-ratio operator can be seen as the absolute value of the logarithm of level $j = 1$ geometric Haar details). First, the approach of [8] can be extended by considering, not only the standard log-ratio operator, but also generalized log-ratio operators (several levels of geometric Haar details for instance). This extension, consisting of an Arithmetic Wavelet transform and Shrinkage of geometric wavelet details $\mathbf{C}^{\times}_{j,n}[\mathcal{P}]$ will be referred as *AWT-SigShrink* $\mathbf{C}^{\times}_{j,n}[\mathcal{P}]$ in the following tests. Change penalization from AWT-SigShrink is provided in Figure 3-[Row 4], when the shrinkage is performed by using sigmoid based functions. AWT-SigShrink change regularization appears suitable mainly for large-size abrupt changes whereas small target change information tends to be blurred by the arithmetic wavelet based regularization.

We then apply the block Sigmoid Shrinkage (notation SigShrink $\mathbf{C}^{\times}_{j,n}[\mathcal{P}]$) given by Eq. (36) directly on the change-images of Figure 3-[Row 3]. This SigShrink operator yields change-images of Figure 3-[Row 5]. As it can be seen in Figure 3-[Row 5], a direct sigmoid shrinkage less impacts the sizes of small structures because it does not involve the smoothing effect intrinsic to wavelet based regularization (compare Figure 3-[Row 5] with the change masks of Figure 3-[Row 2]).

Finally, a comparison based on Receiver Operating Characteristic (ROC, probability of detection versus probability of false alarm for threshold values ranging from minimal to maximal change-image values, see Figure 4) measurements illustrate the advantages and limitations of both approaches:

- for more than 20% of false positives (high toleration of false positives!), then AWT-SigShrink is slightly preferable than SigShrink,
- for less than 20% of false positives, the SigShrink probability of detection is higher than that of AWT-SigShrink, ..., for example, at 5% of false positives, AWT-SigShrink yields 60% of true positives whereas SigShrink yields 80% of true positives.

Thus, for change information enhancement, a direct block sigmoid shrinkage (SigShrink) is preferable than an arithmetic wavelet based regularization (AWT-SigShrink), especially when we have no *a priori* on the sizes and the types of changes (case of glacier surface monitoring addressed hereafter).

V. Geometric wavelets for joint change detection and regularization of polarimetric SAR image time series

A. Block sigmoid shrinkage of polarimetry vectors/matrices

We consider a PolSAR scattering/covariance image time series $\mathcal{P} = \left(\mathcal{P}^{uv}_{m,q}(k)\right)$, where:

- $(u, v) \in \{H, V\} \times \{H, V\}$, H/V stands for *Horizontal* / *Vertical* respectively and
- $([m, q], k)$ refer to (spatial, time) variables, with $1 \leqslant m \leqslant M$, $1 \leqslant q \leqslant Q$ and $1 \leqslant k \leqslant K$.

We have $\mathcal{P}^{uv}_{m,q}(k) = \mathcal{I}^{uv}_{m,q}(k)\Theta^{uv}_{m,q}(k)$ where $\mathcal{I}$ denotes moduli and Θ stands for unit-norm complex exponential phase terms. The temporal geometric wavelet transform is chosen to apply on $\mathcal{I}^{uv}_{m,q}(\bullet)$: the transform is performed to decompose series $\mathcal{I}^{uv}_{m,q}(k)$ with respect to the time variable k solely. Terms $\Theta^{uv}_{m,q}(k)$ are stored and added after regularization of moduli time series $\mathcal{I}$.

Section IV has shown that spatio-temporal block shrinkage of geometric change-images makes change enhancement possible. For polarimetry images, the geometric wavelet transform is chosen to be separable with respect to polarimetry channels whereas the shrinkage of Eq. (36) can be either:

- *scalar*

$$\delta_{\tau,\theta,\lambda}(Z^{uv}_{m,q}(k)) = \frac{\operatorname{sgn}(Z^{uv}_{m,q}(k))(|Z^{uv}_{m,q}(k)| - \tau)_+}{1 + e^{-\zeta(\theta)\left(\frac{\left\|V_{Z^{uv}_{m,q}(k)}\right\|_2}{\lambda} - 1\right)}} \quad (37)$$

  where $Z^{uv}_{m,q}(k)$ is a pixel moduli pertaining to a log-scaled PolSAR change-image.
- or vectorial where neighborhood V consists of ℓ^p norms of PolSAR covariance moduli vector/matrix change-images:

$$\delta_{\tau,\theta,\lambda}(Z^{uv}_{m,q}(k)) = \frac{\operatorname{sgn}(Z^{uv}_{m,q}(k))(|Z^{uv}_{m,q}(k)| - \tau)_+}{1 + e^{-\zeta(\theta)U(Z_{m,q}(k),\lambda)}} \quad (38)$$

where

$$U(Z_{m,q}(k),\lambda) = \left(\frac{\left\| \left\| V_{\left\| \left(Z^{uv}_{m,q}(k) \right)_{(u,v)\in\{H,V\}^2} \right\|_p} \right\|_2}{\lambda} - 1 \right)$$

The time series regularization principle is then to use shrunken geometric wavelet change-images for reconstructing a time series with sharp pixel change transitions. This is the joint parsimonious change evaluation and time series regularization proposed in this paper. We will use the following parameters for block sigmoid shrinkage: $p = 1$, parameter τ_0 is the universal threshold of [35], $\theta = \pi/5$ and $\lambda \in \{\lambda_1, \lambda_2\}$, where $\lambda_1 = \tau_0$, $\lambda_2 = 2\tau_0$. The sigmoid shrinkage operator is denoted $\mathcal{S}^\lambda$.

Note that when 2^J PolSAR image samples are available, then, by restricting the wavelet transform to the time axis and by performing a level J decomposition, we have to take into account the levels $j = 1, 2, \ldots, J$ change-images, with 2^{J-j} change-images at decomposition level $j \leqslant J$ (decimation in order to reject redundant change information).

The overall computational complexity depends on 2 main factors and remains reasonable since it relies only on basic operations (does not involve curves fitting, iterative optimization procedures or maximum likelihood solutions):

- applying a temporal wavelet transform ($M \times Q \times \mathcal{O}(K)$ for the orthogonal transform and $M \times Q \times \mathcal{O}(K^2)$ for non-decimated/stationary versions of the transform) on the logarithms of each moduli of the input time series and using an inverse wavelet transform (same complexity as the decomposition);
- applying a pixelwise shrinkage function involving sums and exponentiations on a small spatial change-image pixel neighborhood (3×3).

Note also that the method is highly parallelizable since the sole recursion is linked to a single axis: the temporal axis concerned by the wavelet transform.

B. Application to Sentinel-1A dual-polarimetric SAR image time series

The geometric temporal wavelet shrinkage for both change information enhancement and time series regularization aims at simplifying the analysis of long series of SAR images. Indeed, the challenge in exploiting such huge data is in dimensionality handling and requires methods that have very low computational load.

Sentinel constellation of the European Space Agency (ESA) is a source of such long time image sequences. The data considered in this section corresponds to an area covering the glaciers *Mer de Glace* and *Argentière*, in the mountainous Chamonix-Mont-Blanc site, in France.

Since the launch of Sentinel-1A in April 2014, a time series of PolSAR data over this test site has been acquired: the test dataset is described in Figure 5 (images are available free of charge from ESA repository). This time series, denoted $\mathcal{P}$, is composed of 11 dual PolSAR IW level-1 Single Look Complex (SLC) SAR images acquired in descending pass from November 15, 2014 to March 15, 2015 with 12 days sampling period. Co-registration of image samples has been made thanks to a corner reflector fixed on a stable area of the test site. A sample image, $\mathcal{P}_2$, is displayed in Figure 5 with a Pauli color rendering in order to enhance dual-polarimetry information.

Different types of changes can occur on this glacier site due to the long period of observation: for instance snow fall, snow accumulation in specific areas, serac falls, avalanches, human activities, *etc.* It is worth noticing that a pixel-per-pixel and date-per-date search is possible, see for instance [36]. However, this is with very high computational cost, in comparison with the geometric temporal wavelet shrinkage proposed below. Specifically, we consider both scalar sigmoid shrinkage (polarimetry channels are considered independently for building V_Z in Eq. (36)) and vector sigmoid shrinkage (V_Z is a sequence of ℓ_p-norms of PolSAR channels) for comparison purpose.

Change information from geometric wavelets:
Due to the limited size of the paper, only one geometric wavelet change-image is displayed in Figure 6-Top. As expected, the details look stochastic, except in few areas. Some areas where significant changes appear in Figure 6-Top are indicated on the photographic map of Figure 6-Bottom:

- a serac fall area on the Argentière glacier (blue-line),
- an accumulation area near the glacier of Bossons (yellow-dashed),
- the borders of glacier Mer de Glace (magenta-dotted).

Changes detected on the borders of *Mer de glace* glacier can be due to co-registration errors. However, since Argentière glacier borders do not respond equivalently, this suspicious behavior needs to be confronted with ground truth because these change responses can reveal other phenomena such as glacier and moraine constriction.

Change enhancement:
Scalar sigmoid shrinkage (polarimetry channels are considered independently) of Figure 6-Top yields the change-image given by Figure 7-Top whereas vector sigmoid shrinkage leads to the change-image of Figure 7-Bottom. One can notice that the latter enhances more accurately polarimetry change information than the former.

Specifically, we also provide:

- in Figure 8-Top, the AWT version of GWT change-image given by Figure 6-Top and
- in Figure 8-Bottom, the AWT version of GWT vector sigmoid shrinkage given by Figure 7-Bottom.

A straightforward comparison of the results obtained highlights that: in multiplicative SAR interactions, the AWT change-image is far from showing only details (images displayed in Figure 6-Top exhibit many contributions of the static part of the scene). This has been justified theoretically in Sections II and IV in terms of non-stationarity and non-sparsity of AWT details, when decomposing signals corrupted by multiplicative noise.

Regularization:
By applying inverse geometric wavelet transform on shrunken change-images, we derive 2 regularized time series (for scalar and vector sigmoid cases) whose sample examples are given by Figure 9. The comparison of images given by Figures 5 and 9 emphasizes nice PolSAR information enhancement for the vector sigmoid geometric wavelet processing.

C. Application to Dynamic-versus-Stable area detection in TerraSAR-X image time series

The following addresses multi-date cumulative geometric wavelet based *change dynamics* analysis over Argentière glacier. The serac fall region of this glacier (see the surface dashed in blue color on Figure 6-Bottom) is a highly dynamic surface surrounded by stable rock areas. This region is considered hereafter in the framework of separability, in terms of *change occurrence count*, between glacier surface [dynamic, changes in texture in addition with glacier moving] *versus* rock walls [stable when observed over a long temporal horizon].

Data description:
The time series $\mathcal{L}$ considered for analyzing change dynamics consists of 24 single look ascending TerraSAR-X (TSX) images acquired over Argentière from 2009/11/06 to 2011/09/14 (images are with 2 meter spatial resolution and are acquired upon 11 days satellite revisit time). Figure 10 provides some samples of $\mathcal{L}$. The 5 first images of Figure 10 are given for instance and the sixth image (detection image D deduced from Argentière's geophysics and expert knowledge) is a ground truth showing:

- [in white color]: glacier surface surrounding a serac fall area (glacier surface moves approximately 20 cm per day). At the serac fall area located on the middle-top of image D, the glacier surface texture is subject to chaotic dynamics and can be assumed as permanently changing between consecutive image acquisitions ;
- [in black color]: an almost stable area composed by abrupt rocks, rock walls and sparse vegetation.

The issue addressed below is a multi-temporal analysis for detecting the *permanently changing* area (glacier) against the *almost stable* area ('non-glacier').

Experimental setup:

The experimental framework aims to compute dissimilarity maps highlighting the total amount of changes encountered from the first image $\mathcal{L}(t_1)$ to the last image $\mathcal{L}(t_{24})$. For the sake of avoiding a biased performance assessment, we do not fix the decision threshold: we will compute, for every method, ROC curves and areas under ROC curves as quantitative detection performance indicators.

Concerning the methods, we will provide comparisons between GWT and AWT SigShrinks, as well as comparisons involving the following change indicators (with the convention: similar is 0 and dissimilar is 1):

- A dissimilarity measure $1 - r$ involving the local correlation coefficient r on pixels of pairs $(\mathcal{L}_m, \mathcal{L}_{m+1})$. This measure will be called "*Dmap CorrCoeff*" in the following. For a change-analysis at pixel level, we consider spatial 3×3 boxcar neighborhood on pixels of pairs $(\mathcal{L}_m, \mathcal{L}_{m+1})$;
- The log-ratio dissimilarity measure between $\mathcal{L}_m$ and $\mathcal{L}_{m+1}$. This measure (see [8] for instance) is defined as the absolute value of the log operator on local pixel ratios. It is denoted "*Dmap LogRatio*" and we consider averaging the log-ratio values obtained on a spatial 3×3 boxcar neighborhood ;
- The coefficient of variation measure considered in the framework of [21] (the coefficient of variation is defined as the ratio between the local standard deviations and means). This measure is denoted "*Dmap CoeffVarr-2-Steps*" due to that the method proposed in [21] is a two stage spatio-temporal change analysis: the first step is a pre-detection (associated with $3 \times 3 \times 3$ spatio-temporal neighborhoods hereafter) and the second step is a detection-refinement (purely temporal non-local analysis from the pre-detection results), see [21] for details.

For all methods, the global dissimilarity is obtained by pairwise dissimilarity sums. In addition, we will not consider post-processing (such as regularization of change maps). This is a supplemental but different issue which can be addressed in a future work.

The experimental setup is the following for GWT and AWT SigShrinks: we consider a Haar wavelet with 3 maximum decomposition levels (the time series $\mathcal{L}$ has 24 images and the maximum decomposition level, $J = 3$, is such that 2^J divides 24). The SigShrink operator is applied on spatial 3×3 wavelet change-image neighborhoods. The parameters of the SigShrink operator are $\tau = 0$, $\theta = \pi/4$ and λ is the universal threshold.

Experimental results:
Dissimilarity maps for CorrCoeff, AWT-SigShrink, LogRatio, CoeffVar-2-Steps and GWT-SigShrink are given by Figure 11. Performance of the corresponding change detections can be measured by using quantities such as:

TABLE I
AUROC CURVE MEASURES THE DIFFERENT DISSIMILARITY MEASURES GIVEN IN SECTION V-C. THE ROC CURVES HAVE BEEN COMPUTED ON THE BASIS OF THE TOTAL AMOUNT OF CHANGES DETECTED IN THE TSX IMAGE TIME SERIES $\mathcal{L}(t_1), \mathcal{L}(t_2), \ldots, \mathcal{L}(t_{24})$ DESCRIBED IN SECTION V-C (SEE SAMPLES GIVEN IN FIGURE 10).

CorrCoeff	AWT-SigShrink-J3	LogRatio	CoeffVar-2-Steps	GWT SigShrink-J1	GWT SigShrink-J3
58.22%	63.69%	68.53%	72.25%	73.21%	75.98%

- the true positive rate associated with a given small false positive rate ('small' means 'no larger than 10%' in most of detection applications). This constrained true positive rate indicator is called TPR[FA$<$ 10%]: a large TPR[FA$<$ 10%] is preferable.
- the *Area Under* ROC (AUROC) curve. A large AUROC is expected to provide a better performance.

For AWT and GWT SigShrinks, we observe increasing performance as the maximal decomposition level varies from 1 to 3. AWT-SigShrink (results are shown only for $J = 3$ in Figure 11) shows worst multi-temporal change detection performance, see ROC curves of Figure 12 and AUROCs given in Table I. One can note, by comparing results given in Figure 12 and AUROCs given in Table I, that GWT less-relevant-detection (obtained for $J = 1$) is more accurate than AWT best detection results (obtained for $J = 3$). From an overall analysis, one can conclude that GWT SigShrink with $J = 3$ is the best relevant strategy both in terms of TPR[FA$<$ 10%] and AUROC performance indicators, see Figure 12 and AUROCs given in Table I for validation.

VI. CONCLUSION

This paper has introduced the concept of geometric wavelet transform by inference between additive and multiplicative algebras. The paper has also derived statistical properties of wavelets in both arithmetic (standard) and geometric implementation frameworks. In the multiplicative-noise observation model, the paper has shown that:

- arithmetic detail wavelet coefficients are impacted by the presence of signal trend (large amounts of signal contribution in detail coefficients), whereas few signal contributions occur in geometric detail coefficients.
- geometric wavelets inherit stationary properties of the input noise whereas additive stationary noise becomes non-stationary in the arithmetic wavelet domain (impact of signal trend in detail coefficients).

Moreover, the paper has shown that the statistical properties of geometric wavelets make them good candidates for the analysis of SAR image time series: in contrast with arithmetic wavelets change-images, geometric wavelet ones are with large amplitudes only near change locations (singularities, transient signal). Change analysis and time series regularization can thus be performed with high performance and low computational complexity by using block shrinkage on geometric wavelet coefficients. Experimental results on both synthetic and real data have shown the relevancy of block shrinkage on geometric wavelet coefficients for both change analysis and time series regularization.

To conclude, it is worth emphasizing that this study was focused on geometric approaches because of the intrinsic multiplicative nature of SAR interactions. Since the geometric wavelet analysis is a framework that extends Log-Ratio operators by considering wavelet based multiresolution ratioing, one can investigate different strategies for the sake of refining multi-resolution ratios and fusing their corresponding detections: this refinement is a regularization of changes which will be addressed in future works.

ACKNOWLEDGMENTS

The authors address special thanks to TGRS anonymous reviewers for their constructive comments and insightful advices on this paper. The authors are very grateful to Sophie Reed who improved the English of this paper. The authors wish also to thank the German Space Agency (DLR) for providing the TerraSAR-X data.

REFERENCES

[1] H. Xie, L. E. Pierce, and F. T. Ulaby, "Statistical properties of logarithmically tranformed speckle," *IEEE Transactions on Geoscience and Remote Sensing*, vol. 40, no. 3, pp. 721 – 727, Mar. 2002.

[2] R. Garcia, T. Nicosevici, and X. Cufi, "On the way to solve lighting problems in underwater imaging," in *OCEANS '02 MTS/IEEE*, vol. 2, 2002, pp. 1018–1024 vol.2.

[3] O. Michailovich and A. Tannenbaum, "Despeckling of medical ultrasound images," *Ultrasonics, Ferroelectrics and Frequency Control, IEEE Transactions on*, vol. 53, no. 1, pp. 64–78, 2006.

[4] L. Florack and H. Assen, "Multiplicative calculus in biomedical image analysis," *Journal of Mathematical Imaging and Vision*, vol. 42, no. 1, pp. 64–75, 2012. [Online]. Available: http://dx.doi.org/10.1007/s10851-011-0275-1

[5] P. Gould and F. Vahid-Araghi, "Time series with multiple seasonal patterns," in *Forecasting with Exponential Smoothing*, ser. Springer Series in Statistics. Springer Berlin Heidelberg, 2008, pp. 229–254. [Online]. Available: http://dx.doi.org/10.1007/978-3-540-71918-2_14

[6] M. Verbeek, *A Guide to Modern Econometrics, 4th Edition*. John Wiley & Sons, February 2012.

[7] J. M. Box-Steffensmeier and C. J. W. Zorn, "Duration models and proportional hazards in political science." Springer Berlin Heidelberg, 2001, vol. 45, no. 4, pp. 972–988.

[8] C. Marin, F. Bovolo, and L. Bruzzone, "Building change detection in multitemporal very high resolution SAR images," *IEEE Trans. Geosci. Remote Sens.*, vol. 53, no. 5, pp. 2664–2682, 2015.

[9] W. Yang, H. Song, G.-S. Xia, and C. Lopez-Martinez, "Dissimilarity measurements for processing and analyzing PolSAR data: A survey," *in Proc. IGARSS Milan, Italy*, pp. 1562–1565, 2015.

[10] G. Quin, B. Pinel-Puyssegur, J.-M. Nicolas, and P. Loreaux, "MIMOSA: An automatic change detection method for SAR time series," *IEEE Trans. Geosci. Remote Sens*, vol. 52, no. 9, pp. 5349–5363, 2014.

[11] G. Liu and H. Zhong, "Nonlocal means filter for polarimetric SAR despeckling based on discriminative similarity measure," *IEEE Geosci. Remote Sens. Lett.*, vol. 11, no. 2, pp. 514–518, 2014.

[12] A. C. Frery, A. D. C. Nascimento, and R. J. Cintra, "Analytic expressions for stochastic distances between relaxed complex Wishart distributions," *IEEE Trans. Geosci. Remote Sens.*, vol. 52, no. 2, pp. 1213–1226, 2014.

[13] A. M. Atto, E. Trouvé, Y. Berthoumieu, and G. Mercier, "Multidate divergence matrices for the analysis of sar image time series," *IEEE Transactions on Geoscience and Remote Sensing*, vol. 51, no. 4, pp. 1922–1938, April 2013. [Online]. Available: http://dx.doi.org/10.1109/TGRS.2012.2210228

[14] M. Dabboor, M. J. Collins, V. Karathanassi, and A. Braun, "An unsupervised classification approach for polarimetric SAR data based on the Chernoff distance for complex Wishart distribution," *IEEE Trans. Geosci. Remote Sens.*, vol. 51, no. 7, pp. 4200–4213, 2013.

[15] G. Quin, B. Pinel-Puyssegur, and J.-M. Nicolas, "Comparison of harmonic, geometric and arithmetic means for change detection in SAR time series," *EUSAR*, 2012.

[16] E. Trouvé, Y. Chambenoit, N. Classeau, and P. Bolon, "Statistical and operational performance assessment of multitemporal SAR image filtering." *IEEE Trans. Geosci. Remote Sens.*, vol. 41, no. 11, pp. 2519–2530, 2003.

[17] R. Touzi, "A review of speckle filtering in the context of estimation theory," *IEEE Trans. Geosci. Remote Sens.*, vol. 40, no. 11, p. 23922404, 2002.

[18] A. Gar-OnYeh and Z. Qi, *Space-Time Integration in Geography and GIScience. Chapter 19: Short-Interval Monitoring of Land Use and Land Cover Change Using a Time Series of RADARSAT-2 Polarimetric SAR Images.* Springer Link, 2015.

[19] X. Su, C. Deledalle, F. Tupin, and H. Sun, "Two-step multitemporal nonlocal means for synthetic aperture radar images," *IEEE Trans. Geosci. Remote Sens.*, vol. 52, no. 10, pp. 6181 – 6196, 2014.

[20] V. Akbari, A. P. Doulgeris, and T. Eltoft, "Monitoring glacier changes using multitemporal multipolarization SAR images," *IEEE Trans. Geosci. Remote Sens.*, vol. 52, no. 6, pp. 3729–3741, 2014.

[21] T. T. Lê, A. M. Atto, E. Trouvé, and J.-M. Nicolas, "Adaptive multitemporal SAR image filtering based on the change detection matrix," *IEEE Geoscience and Remote Sensing Letters*, vol. 11, no. 10, pp. 1826–1830, Oct 2014.

[22] T. Schellenberger, B. Ventura, M. Zebisch, and C. Notarnicola, "Wet snow cover mapping agorithm based on multitemporal COSMO-SkyMed X-band SAR images," *IEEE J. Sel. Topics Appl. Earth Observations Remote Sens.*, vol. 5, no. 3, pp. 1045–1053, 2012.

[23] X. Xing, Z. Chen, H. Zou, and S. Zhou, "Statistical assessment of model fit for SAR sea clutter," *in Proc. SPIE*, vol. 7494, 2009.

[24] S. Quegan, T. L. Toan, J. J. Y. Jiong, F. Ribbes, and N. Floury, "Multitemporal ERS SAR analysis applied to forest mapping," *IEEE Trans. Geosci. Remote Sens.*, vol. 38 , no. 2, pp. 741–753, 2000.

[25] J. Lehtiranta, S. Siiria, and J. Karvonen, "Comparing C- and L-band SAR images for sea ice motion estimation," *The Cryosphere*, vol. 9, pp. 357–366, 2015.

[26] A. Alonso-Gonzalez, C. Lopez-Martinez, and P. Salembier, "Filtering and segmentation of polarimetric SAR data based on binary partition trees," *IEEE Trans. Geosci. Remote Sens.*, vol. 50, no. 2, pp. 593–605, 2012.

[27] D. Amitrano, F. Ciervo, P. D. Bianco, G. D. Martino, A. Iodice, F. Mitidieri, D. Riccio, G. Ruello, M. N.Papa, and Y. Koussoube, "Monitoring soil erosion and reservoir sedimentation in semi-arid region through remote sensed SAR data: A case study in Yatenga region, Burkina Faso," *Engineering Geology for Society and Territory, Springer link*, vol. 3, pp. 539–542, 2015.

[28] H. Zhong, Y. Li, and L. Jiao, "SAR image despeckling using bayesian nonlocal means filter with sigma preselection," *IEEE Geosci. Remote Sens. Lett.*, vol. 8, no. 4, pp. 809–813, 2011.

[29] S. Parrilli, M. Poderico, C. V. Angelino, and L. Verdoliva, "A nonlocal SAR image denoising algorithm based on LLMMSE wavelet shrinkage," *IEEE Trans. Geosci. Remote Sens.*, vol. 50, no. 2, pp. 606–616, 2012.

[30] A. M. Atto, D. Pastor, and G. Mercier, "Wavelet shrinkage: Unification of basic thresholding functions and thresholds," *Signal, Image and Video Processing, Springer*, vol. 5, no. 1, pp. 11 – 28, 2011. [Online]. Available: http://dx.doi.org/10.1007/s11760-009-0139-y

[31] S. Mallat, *A wavelet tour of signal processing, second edition.* Academic Press, 1999.

[32] I. Daubechies, *Ten lectures on wavelets.* SIAM, Philadelphie, PA, 1992.

[33] R. R. Coifman and D. L. Donoho, *Translation invariant denoising.* Lecture Notes in Statistics, 1995, no. 103, pp. 125 – 150.

[34] A. M. Atto and Y. Berthoumieu, "Wavelet packets of nonstationary random processes: Contributing factors for stationarity and decorrelation," *IEEE Transactions on Information Theory*, vol. 58, no. 1, Jan. 2012. [Online]. Available: http://dx.doi.org/10.1109/TIT.2011.2167496

[35] D. L. Donoho and I. M. Johnstone, "Ideal spatial adaptation by wavelet shrinkage," *Biometrika*, vol. 81, no. 3, pp. 425 – 455, Aug. 1994.

[36] T. T. Lê, A. M. Atto, and E. Trouvé, "Change analysis of dual polarimetric sentinel-1 SAR image time series using stationary wavelet transform and change detection matrix," *8th International Conference on the Analysis of Multitemporal Remote Sensing Images, Annecy, France, July 22 - 24.*

Appendix A
Proof of Proposition 2

By considering the log of $\mathbf{C}^{\times}_{j+1,2n+\epsilon}$ denoted by $\mathbf{D}_{j+1,2n+\epsilon}$, we are concerned by an additive combinations of $\mathbf{D}_{j,n} = \log \mathbf{C}^{\times}_{j,n}$.

The autocorrelation functions

$$R_{\mathbf{D}_{j+1,2n+\epsilon}}[k,\ell] = \mathbb{E}\mathbf{D}_{j+1,2n+\epsilon}[k]\mathbf{D}_{j+1,2n+\epsilon}[\ell]$$

and

$$R_{\mathbf{D}_{j,n}}[k,\ell] = \mathbb{E}\mathbf{D}_{j,n}[k]\mathbf{D}_{j,n}[\ell]$$

of $\mathbf{D}_{j+1,2n+\epsilon}$ and $\mathbf{D}_{j,n}$ satisfy the relation:

$$R_{\mathbf{D}_{j+1,2n+\epsilon}}[k,\ell] = \sum_{p\in\mathbb{Z}}\sum_{q\in\mathbb{Z}} \mathbf{h}_{\epsilon}[p-2k]\mathbf{h}_{\epsilon}[q-2\ell]\times R_{\mathbf{D}_{j,n}}[p,q] \quad (39)$$

Since $\mathbf{D}_{j,n}$ is stationary: $R_{\mathbf{D}_{j,n}}[p,q] \triangleq R_{\mathbf{D}_{j,n}}[p-q]$, then Eq. (39) can be rewritten in the form

$$R_{\mathbf{D}_{j+1,2n+\epsilon}}[k,\ell] = \sum_{p\in\mathbb{Z}} R_{\mathbf{D}_{j,n}}[p]\times \sum_{q\in\mathbb{Z}} \mathbf{h}_{\epsilon}[p+q-2k]\mathbf{h}_{\epsilon}[q-2\ell]. \quad (40)$$

By taking into account that (Parseval's theorem):

$$\sum_{q\in\mathbb{Z}} \mathbf{h}_\epsilon[p+q-2k]\mathbf{h}_\epsilon[q-2\ell] = \sum_{q\in\mathbb{Z}} \tau_{2k-2\ell-p}\mathbf{h}_\epsilon[q]\mathbf{h}_\epsilon[q] = \frac{1}{2\pi}\int_{-\pi}^{\pi} \left|\widehat{H_\epsilon}(\omega)\right|^2 e^{i(2k-2\ell-p)\omega}\,d\omega, \quad (41)$$

we obtain from Eq. (40):

$$R_{\mathbf{D}_{j+1,2n+\epsilon}}[k,\ell] = \frac{1}{2\pi}\int_{-\pi}^{\pi} e^{i(2k-2\ell)\omega}\left|\widehat{\mathbf{H}_\epsilon}(\omega)\right|^2 \times \left(\sum_{p\in\mathbb{Z}} R_{\mathbf{D}_{j,n}}[p]e^{-ip\omega}\right) \quad (42)$$

The proof follows from Eq. (23) and Eq. (42), by identifying the Fourier expansion of $\gamma_{\mathbf{D}_{j,n}}$ in Eq. (42) and by noting that $R_{\mathbf{D}_{j+1,2n+\epsilon}}[p,q] \triangleq R_{\mathbf{D}_{j+1,2n+\epsilon}}[p-q] = R_{\mathbf{D}_{j+1,2n+\epsilon}}[m]$ where $m = k-\ell$.

Appendix B
Proof of Proposition 3

Let $\epsilon \in \{0,1\}$. The Haar scaling filter $\mathbf{H}_0^{\text{Haar}}$ and wavelet filter $\mathbf{H}_1^{\text{Haar}}$ satisfies

$$\mathbf{H}_\epsilon^{\text{Haar}}(\omega) = \frac{1}{2}\left(1+(1-2\epsilon)e^{-i\omega}\right) \quad (43)$$

By taking into account Eqs. (5) and (43), we have

$$\mathbf{H}_{j,n}^{\text{Haar}}(\omega) = 2^{-j/2}\prod_{\ell=1}^{j}\left(1+(1-2\epsilon_\ell)e^{-i\omega}\right). \quad (44)$$

Thus,

$$\left|\mathbf{H}_{j,n}^{\text{Haar}}(\omega)\right|^2 = \prod_{\ell=1}^{j}\left(1+(1-2\epsilon_\ell)\cos(2^{\ell-1}\omega)\right). \quad (45)$$

The proof follows by noting that $(1-2\epsilon_\ell)\cos(2^{\ell-1}\omega) = \cos(2^{\ell-1}\omega+\epsilon_\ell\pi)$ after some straightforward simplifications by using trigonometry double angle properties.

Appendix C
Proof of Proposition 4

From a change of variable in Eq. (29), we obtain

$$R_{\mathbf{D}_{j,0}}^{\text{Haar}}[m] = \frac{1}{\pi}\int_0^{2^j\pi}\left(\frac{\operatorname{sinc}(\omega/2)}{\operatorname{sinc}(\omega/2^{j+1})}\right)^2 \gamma_{\mathbf{Y}}(\frac{\omega}{2^j})\cos m\omega\,d\omega.$$

First, we observe that:

$$\left|R_{\mathbf{D}_{j,0}}^{\text{Haar}}[m]\right| \leqslant \|\gamma_{\mathbf{Y}}\|_\infty \times \left(\frac{1}{\pi}\int_0^{2^j\pi}\left(\frac{\operatorname{sinc}(\omega/2)}{\operatorname{sinc}(\omega/2^{j+1})}\right)^2 d\omega\right).$$

and, furthermore, we have

$$\frac{1}{\pi}\int_0^{+\infty}\left(\frac{\operatorname{sinc}(\omega/2)}{\operatorname{sinc}(\omega/2^{j+1})}\right)^2 d\omega = 1.$$

In this respect, we derive

$$\left|R_{\mathbf{D}_{j,0}}^{\text{Haar}}[m]\right| \leqslant \|\gamma_{\mathbf{Y}}\|_\infty$$

so that, from the Lebesgue dominated convergence theorem,

$$\lim_{j\to+\infty} R_{\mathbf{D}_{j,0}}^{\text{Haar}}[m] = \gamma_{\mathbf{Y}}(0)\frac{1}{\pi}\int_0^{+\infty}(\operatorname{sinc}(\omega/2))^2\cos m\omega\,d\omega$$

Proposition 4 then follows by noting that

$$\int_0^{+\infty}(\operatorname{sinc}(\omega/2))^2\cos m\omega\,d\omega = \pi\delta[m]$$

$\mathcal{P} = \{\mathcal{P}(t_1), \mathcal{P}(t_2), \ldots \mathcal{P}(t_{11})\}$	Data: SAR, Single Look Complex
$t_1 = 2014 - 11 - 15$	Revisit time: 12 days
$t_{11} = 2015 - 03 - 15$	Orbit pass: descending
Dual PolSAR IW level-1	Resolution: 3.5×20 m^2

$\mathcal{P}_1 = \mathcal{P}(t_1)$ with $t_1 = 2014 - 11 - 15$

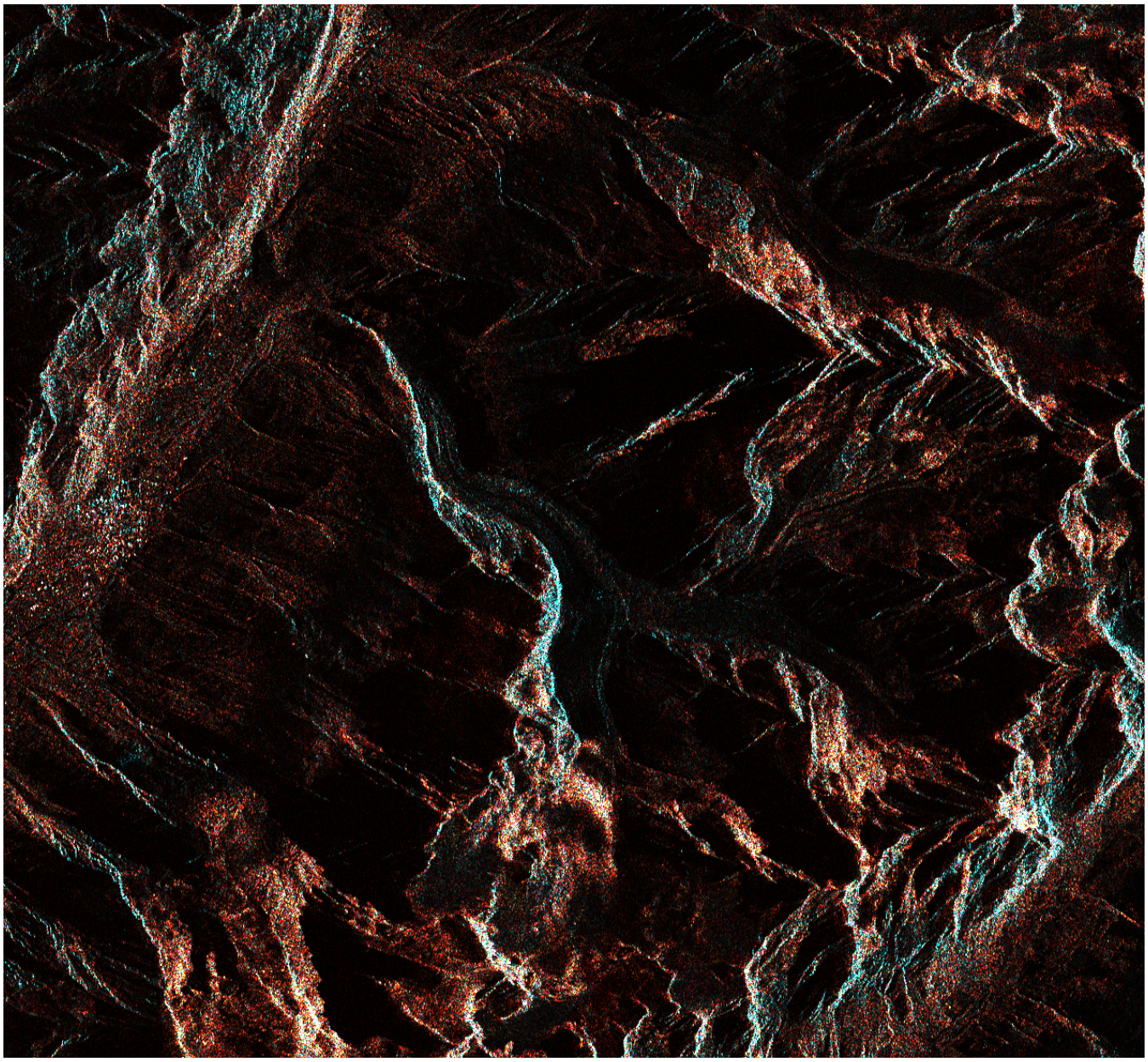

Fig. 5. Sentinel-1A dual PolSAR image of the Chamonix-Mont-Blanc test site.

$\mathcal{D}_{3,1}[\mathcal{P}]$/
Change-image
(GWT details)

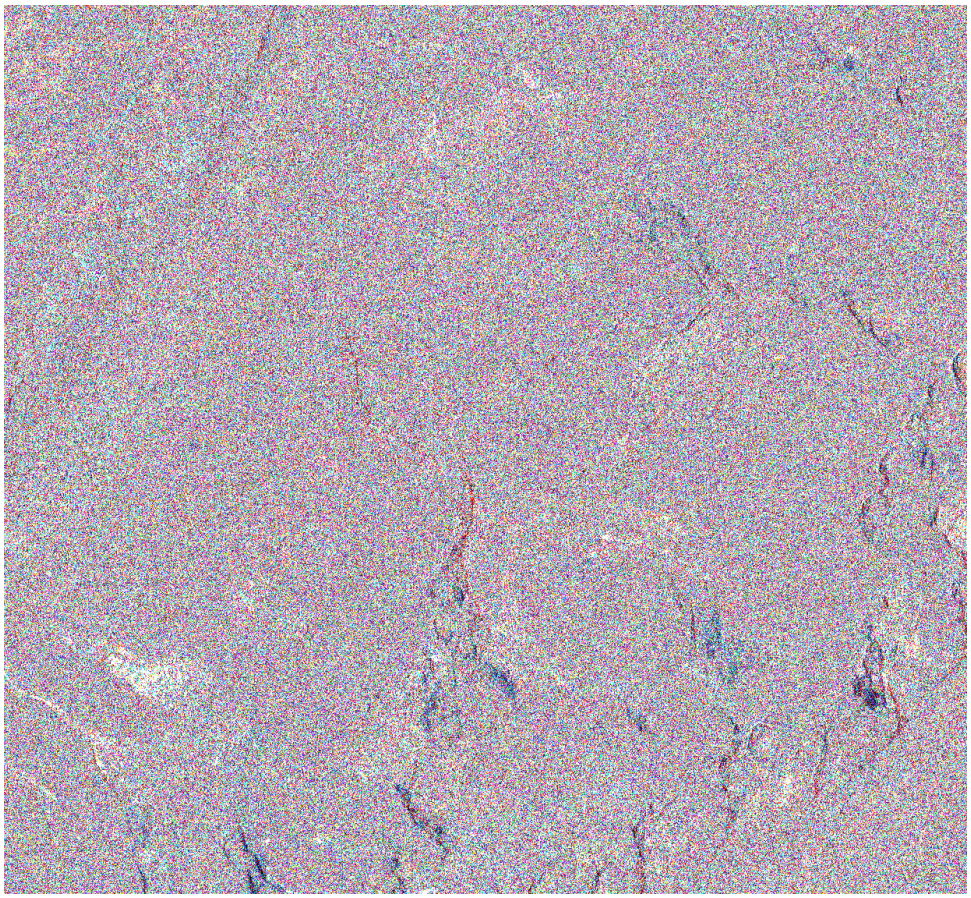

Airborne
photography

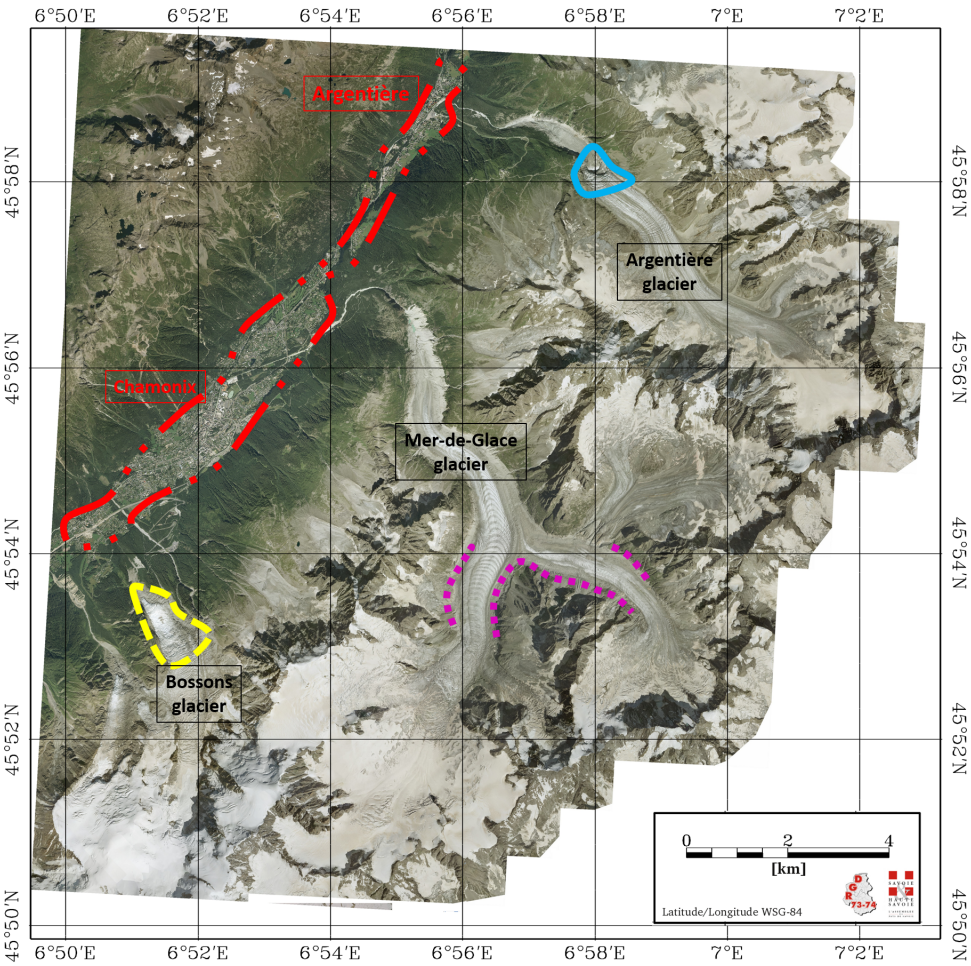

Fig. 6. [Top]: a geometric change-image of PolSAR time series $\mathcal{P}$ described in Figure 5. [Bottom]: airborne photography [©RGD 73-74] showing Chamonix urban valley (red dash-dotted), glaciers (*Argentière*, *Mer de Glace*, *Bossons*) and localization of significant changes.

$\mathcal{D}_{3,1}^{\mathcal{S}_s}[\mathcal{P}]$/
Scalar SigShrink
(GWT details)

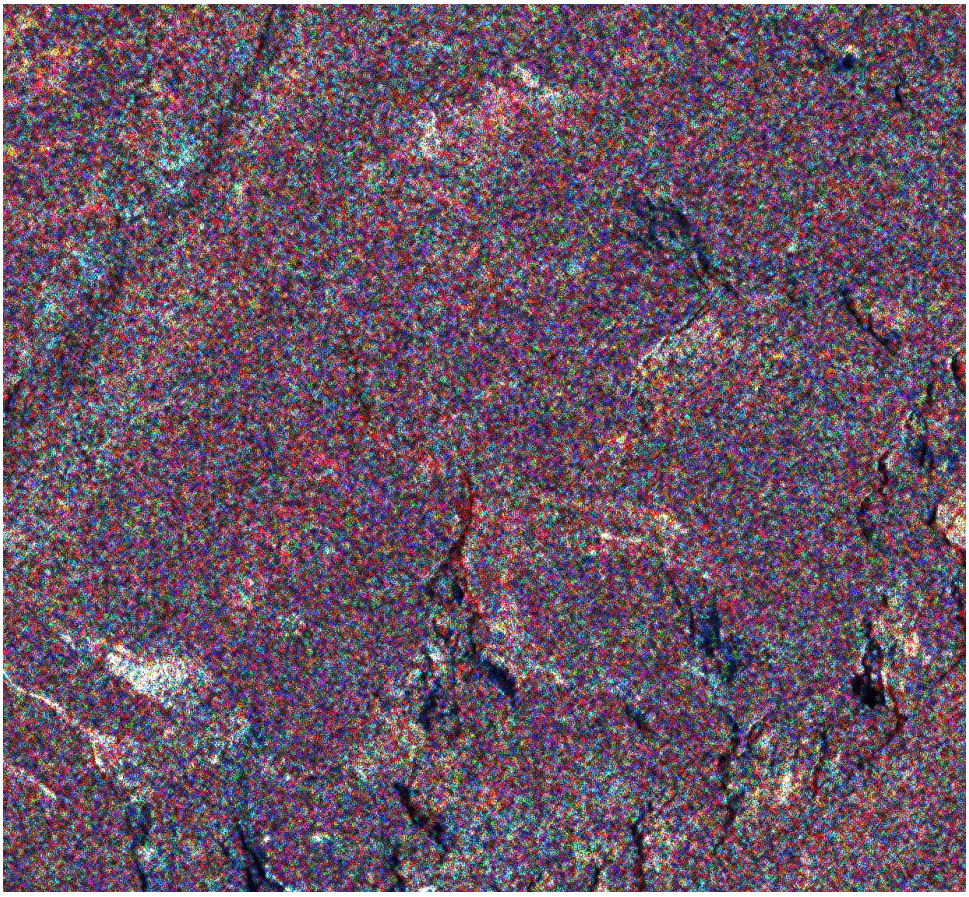

$\mathcal{D}_{3,1}^{\mathcal{S}_v}[\mathcal{P}]$/
Vector SigShrink
(GWT details)

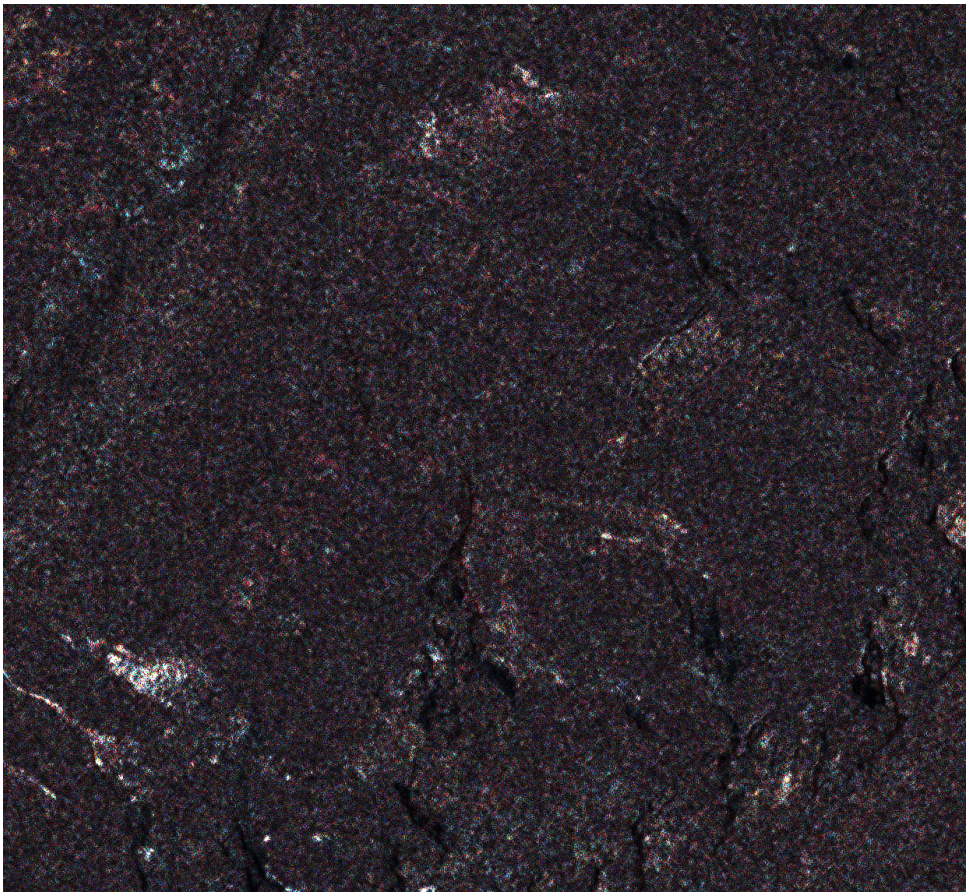

Fig. 7. GWT SigShrink: Scalar (Top, $\mathcal{D}_{3,1}^{\mathcal{S}_s}$) and vector (Bottom, $\mathcal{D}_{3,1}^{\mathcal{S}_v}$) sigmoid shrinkages of the geometric change-image $\mathcal{D}_{3,1}$ given in Figure 6.

$\mathcal{D}_{3,1}[\mathcal{P}]$/
Change-image
(AWT details)

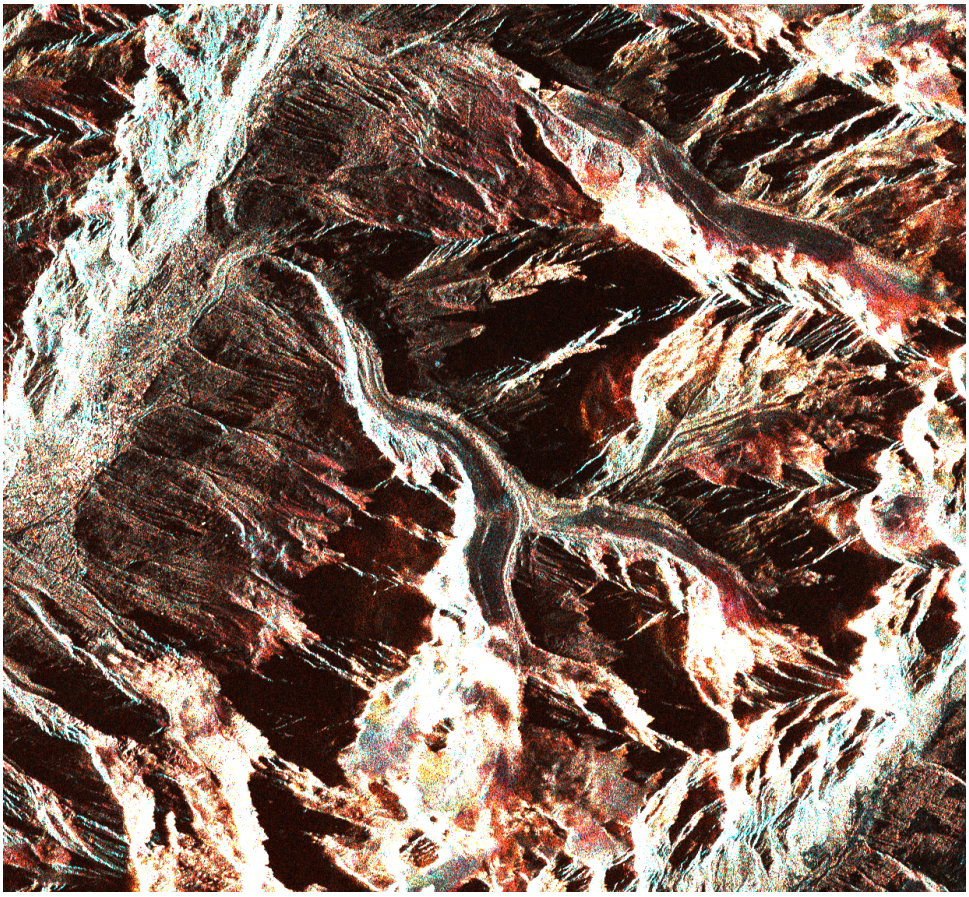

$\mathcal{D}^{\mathcal{S}_v}_{3,1}[\mathcal{P}]$/
Vector SigShrink
(AWT details)

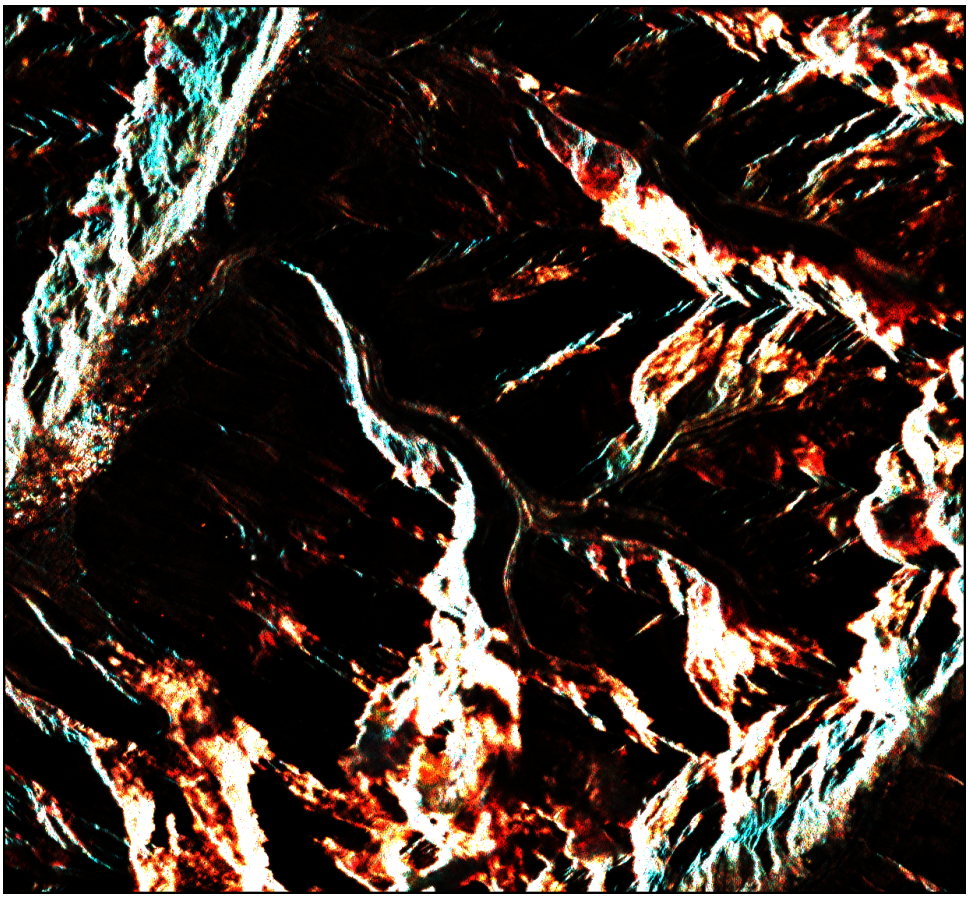

Fig. 8. [Top]: an arithmetic change-image of the PolSAR time series $\mathcal{P}$ described in Figure 5. Compare this AWT change-image (highly non-stationary, impacted by scene trend) with the GWT version (almost stationary, excepted in dynamic areas) given by Figure 6. [Bottom]: vector sigmoid shrinkage of the top image. Compare the bottom image (AWT SighShrink) with its GWT version given in Figure 7-Bottom.

$\widehat{\mathcal{P}}_2^s = \widehat{\mathcal{P}}^s(t_1)$
$t_2 =$
$2014 - 11 - 27$

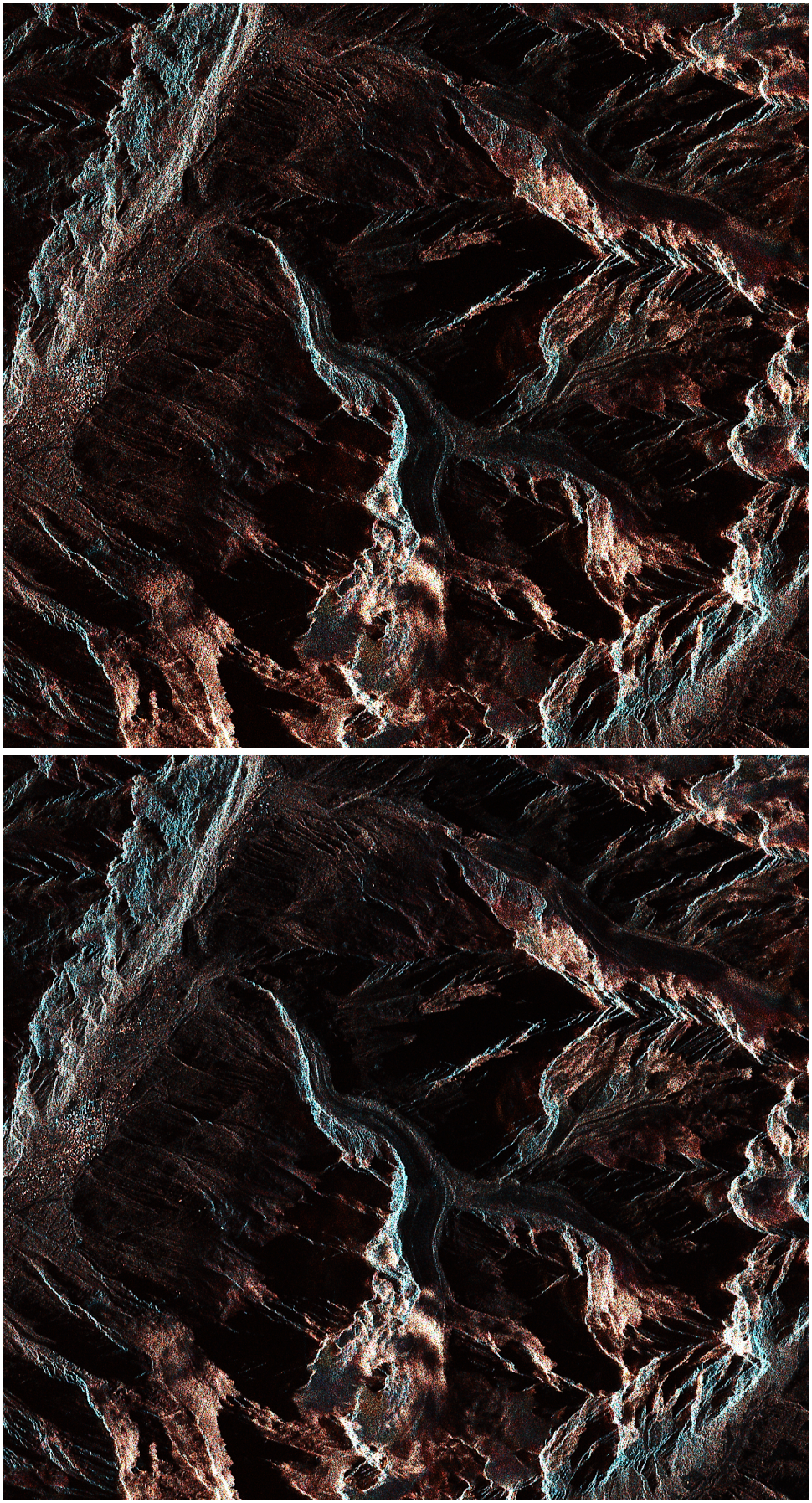

$\widehat{\mathcal{P}}_2^v = \widehat{\mathcal{P}}^v(t_1)$
$t_2 =$
$2014 - 11 - 27$

Fig. 9. Scalar (Top) and vector (Bottom) geometric wavelet regularization of Sentinel-1A PolSAR time series $\mathcal{P}$ described in Figure 5. Scalar shrinkage shows red color saturation, in contrast with vector shrinkage. Compare these regularized images with their corresponding original time sample given in Figure 5.

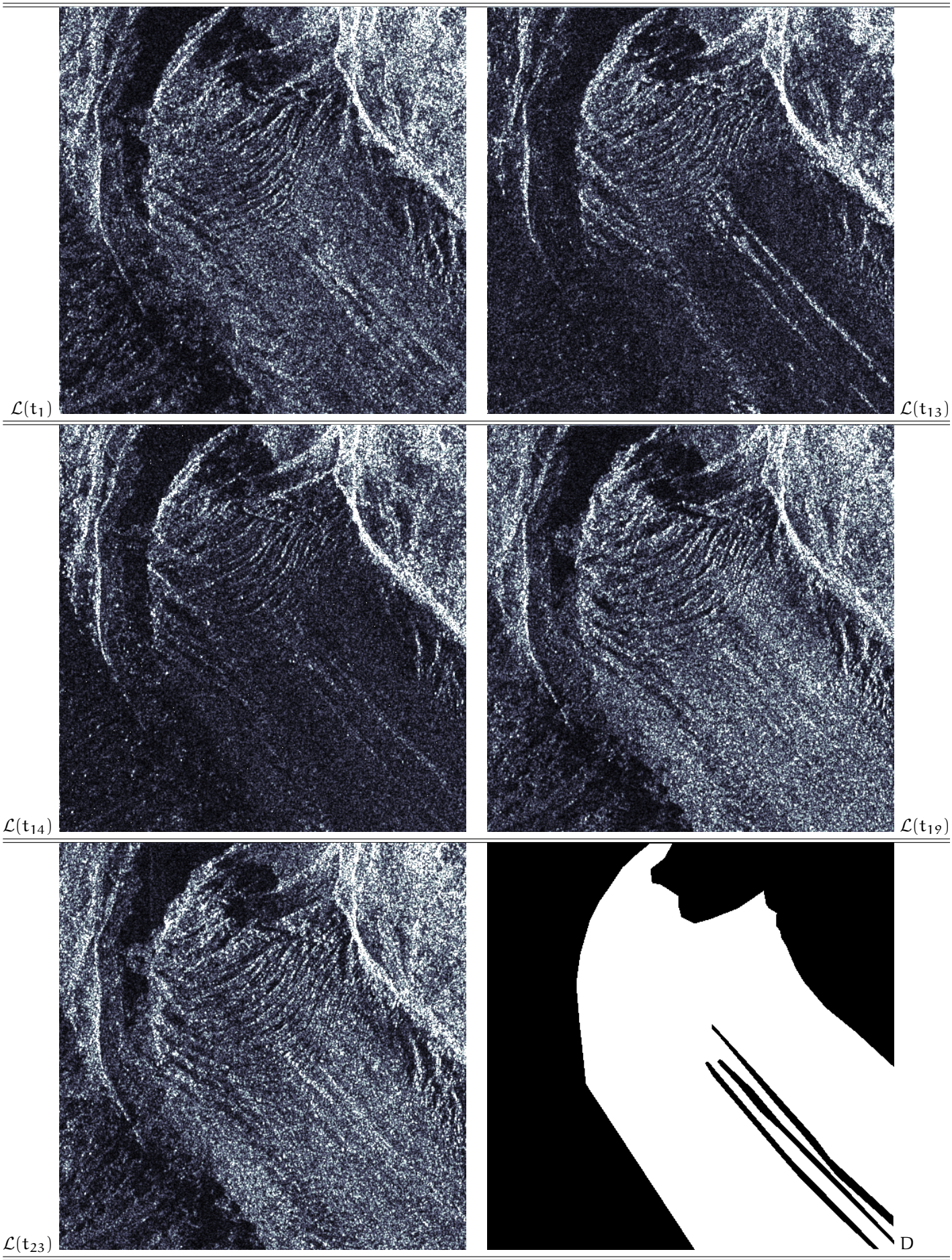

Fig. 10. Five samples of a TSX time series $\mathcal{L} = \{\mathcal{L}(t_1), \mathcal{L}(t_2), \ldots, \mathcal{L}(t_{24})\}$ together with a ground truth D delimiting stable (black) and dynamic (white) pixels. The time series $\mathcal{L}$ is described in Section V-C.

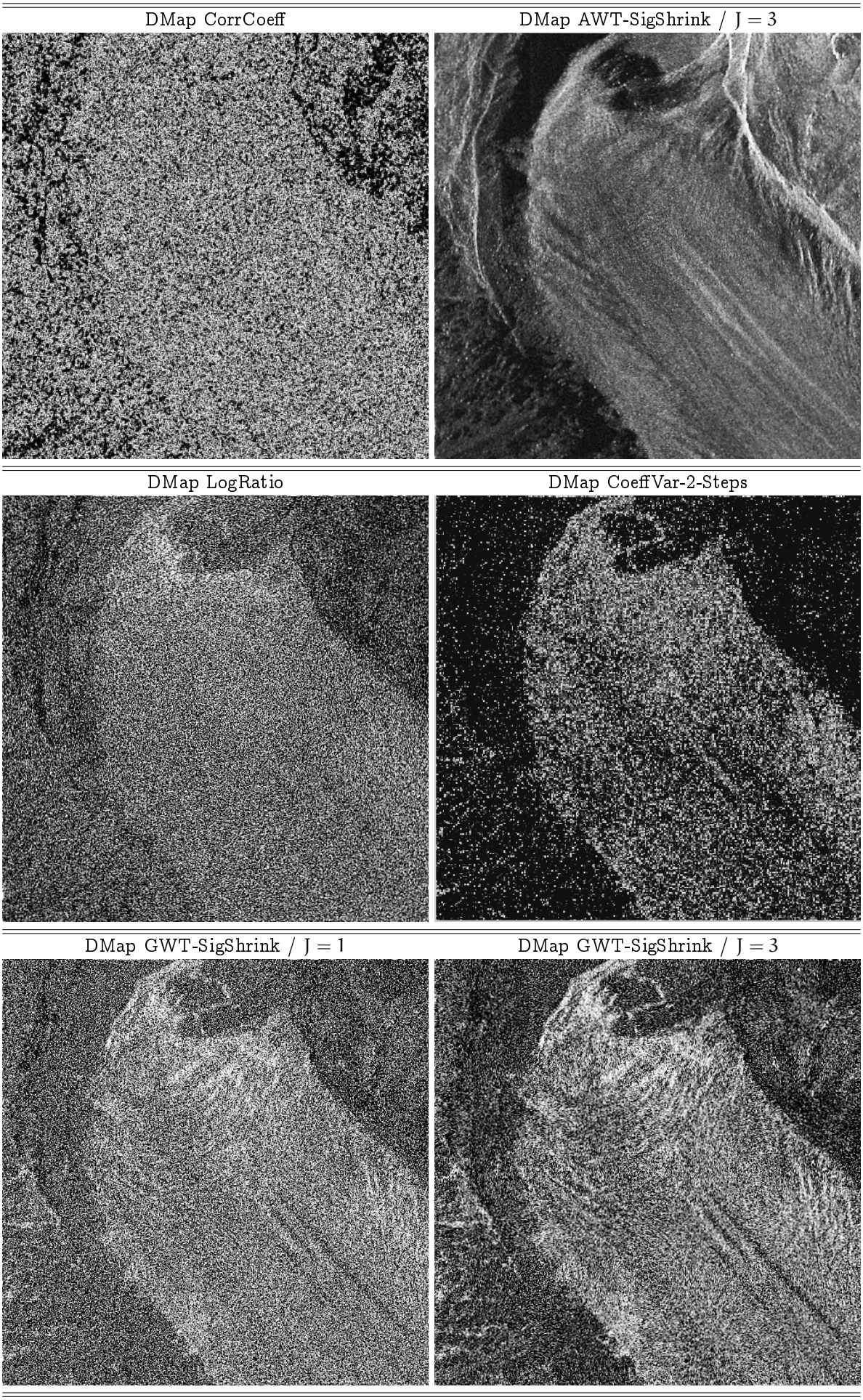

Fig. 11. Dissimilarity maps (Dmaps) for the measures given in Section V-C. Dmaps represent the total amount of changes detected in the TSX image time series $\mathcal{L}(t_1), \mathcal{L}(t_2), \ldots, \mathcal{L}(t_{24})$ described in Section V-C (see samples and ground truth given in Figure 10).

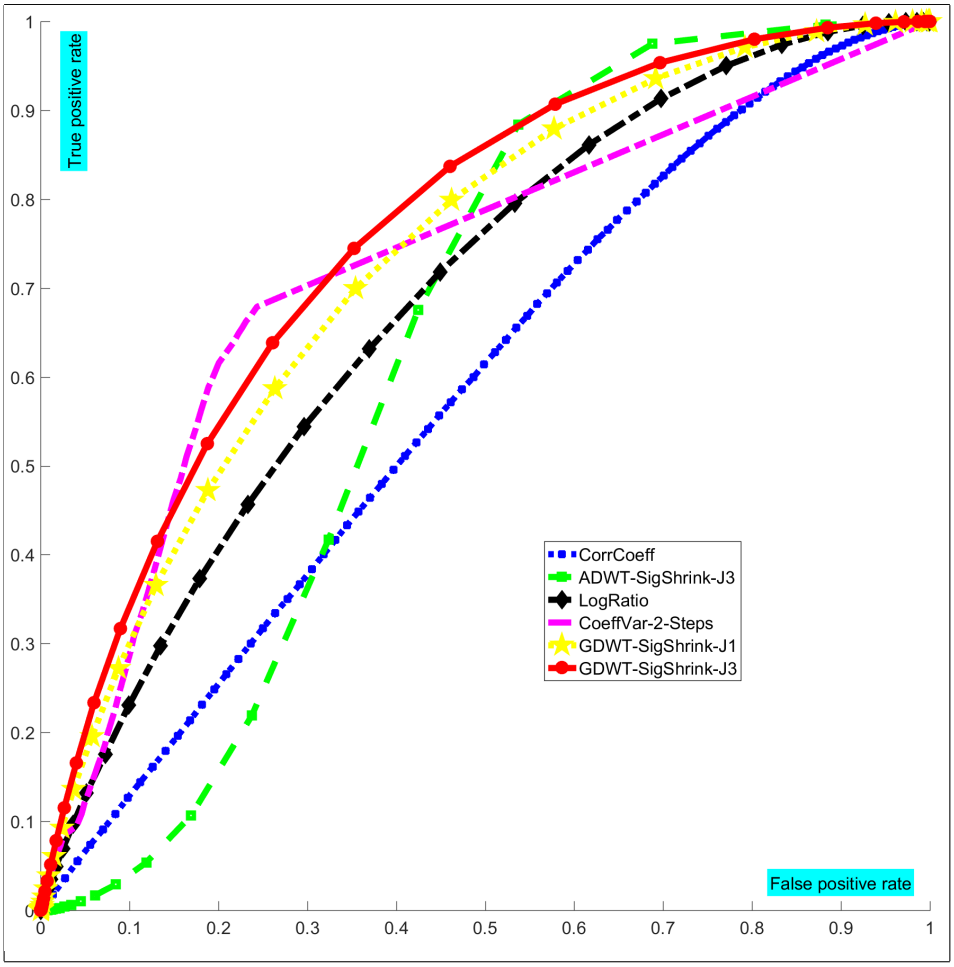

Fig. 12. ROC curves for the different dissimilarity measures given in Section V-C. ROC curves have been computed on the basis of the total amount of changes detected in the TSX image time series $\mathcal{L}(t_1), \mathcal{L}(t_2), \ldots, \mathcal{L}(t_{24})$ described in Section V-C (see samples given in Figure 10).